
Single-Cell Concept Bottleneck Generative Models for Interpretable and Controllable Cellular Editing

Alma Andersson^{*1} Aya Abdelsalam Ismail^{*2} Edward De Brouwer^{*1} Doron Haviv^{*1} Tommaso Biancalani¹
 Kyunghyun Cho¹³⁴ Gabriele Scalia¹ Aicha BenTaieb¹ Hector Corrada Bravo¹

Abstract

Understanding cellular phenotypes and how they respond to perturbations is critical for disease biology and therapeutic design. Single-cell RNA sequencing enables characterization at cellular resolution, yet the combinatorial space of conditions makes exhaustive experimental mapping infeasible. We introduce single-cell Concept Bottleneck Generative Models (scCBGM), a framework for interpretable and precise counterfactual editing of individual cells. scCBGM adapts concept bottleneck architectures for single-cell data through decoder skip connections and a cross-covariance penalty that promotes disentanglement without dimensional constraints. We extend the framework to flow matching models, enabling concept-guided editing in both encoding-decoding and generation regimes. To enable rigorous evaluation, we develop a synthetic benchmark with ground-truth counterfactuals. Across multiple real datasets, scCBGM demonstrates superior performance in combinatorial generalization and counterfactual prediction, supported by cell-level validation on synthetic data and population-level benchmarks on real datasets.

1. Introduction

Understanding cellular phenotypes and how they mediate response to exposures, e.g., drugs, cytokines, chemokines, is critical to disease biology and translational clinical research. Single-cell RNA sequencing (scRNA-seq) enables the characterization of cellular phenotypes and measuring responses

^{*}Equal contribution ¹Genentech ²Guide Labs ³Department of Computer Science, New York University ⁴Center for Data Science, New York University. Correspondence to: Alma Andersson <andersson.alma@gene.com>. Code available at <https://github.com/almaan/scCBGM>.

at cellular resolution, revealing cell states, trajectories, and disease mechanisms (Bergen et al., 2020; Aebermann et al., 2018; Kang et al., 2017; Wu et al., 2021). Yet the combinatorial space of cellular populations and conditions (treatments, exposures, doses) makes exhaustive experimental mapping infeasible (Kana et al., 2023). Computational models that can help fill this map by predicting cellular responses under unseen conditions are therefore essential.

A critical capability required of these models is the ability to perform precise **cellular editing**: starting with an observed cell and systematically modifying specific biological properties while preserving others. Editing differs from conditional generation in that the latter considers *any* cell under given conditions, while the former considers a *specific* cell under altered conditions. For example, a researcher might ask “*What would this T-cell look like after receiving anti-PD-1 or anti-TNF treatment, compared to its observed untreated state? What if its NF- κ B pathway is turned off?*”. Such editing capabilities enable cell-level counterfactual reasoning, which is critical for causal discovery, therapeutic design, and precision medicine.

A cell-editing model must satisfy two requirements. First, it should generate cell-specific counterfactuals, predicting how an observed cell would respond to a specified intervention, rather than only population-level averages. Second, it should provide interpretable control, allowing interventions on biologically meaningful concepts such as gene programs or cell types, rather than opaque latent variables. Earlier methods modeled conditional distributions of cell states across contexts, capturing population-level effects but not counterfactuals for individual cells (Lotfollahi et al., 2019; Kana et al., 2023; Adduri et al., 2025). More recent work has moved toward cell-level counterfactual prediction (Zhang et al., 2024; Piran et al., 2024), but explicit, interpretable control remains an open and important area for further development. Meanwhile, existing interpretability methods are descriptive but not actionable: they explain correlations but cannot simulate or edit cellular responses (Zhao et al., 2021; Chen et al., 2024). Enabling precise counterfactual editing at the level of individual cells with biologically interpretable control remains an open challenge.

In this work, we introduce single-cell Concept Bottleneck Generative Models (scCBGM), a generative framework that enables interpretable and controllable cellular editing. Our approach builds on Concept Bottleneck Generative Models (CBGMs) (Ismail et al., 2023), which extend concept bottleneck models (Koh et al., 2020) to the generative setting, adapting them to the unique challenges of single-cell data: high heterogeneity, complex biological processes, substantial technical noise, and unreliable concept annotations. Our main contributions are:

- We introduce architectural modifications to CBGMs: a computationally efficient cross-covariance penalty that promotes decoupled embeddings without imposing dimensionality constraints on model components and decoder concept skip connections that enable controllable generation under noisy biological annotations.
- We extend scCBGM beyond VAEs to flow matching models, enabling concept-guided editing in both decoding-only and encoding-decoding regimes. This demonstrates the flexibility of our framework across generative architectures.
- We develop a synthetic data generation process that separates exogenous noise from conditions, providing access to true counterfactuals. This enables systematic evaluation of concept-based editing under realistic single-cell settings (noise, missing labels, heterogeneous populations).
- We demonstrate strong cell-level editing accuracy on our synthetic benchmark, where ground-truth counterfactuals are available, and competitive-to-strong performance on population-level proxy metrics across three real-world datasets, outperforming several state-of-the-art methods in combinatorial and zero-shot generalization. We show a use case where in-silico interventions with scCBGM on both cellular phenotype, i.e., pathway activity *and* treatment elucidate mechanistic hypotheses of treatment response.

2. scCBGM Single-Cell Concept Bottleneck Generative Model

This section formalizes the problem of single-cell counterfactual editing, describes the architecture and training objectives of scCBGM, and details a procedure for augmenting flow matching generative models with scCBGM.

2.1. Problem setup

We assume N i.i.d. single-cell RNA-seq profiles $\mathbf{x} \in \mathbb{R}^d$, each with d genes, and an associated vector of K biological concepts $\mathbf{c} \in \mathbb{R}^K$. Each concept may be binary (e.g., cell type or stimulation status, encoded as 0/1) or continuous/soft (e.g., a drug dosage or pathway-activity score). Our

goal is to generate *counterfactual gene expression*: given a factual cell (\mathbf{x}, \mathbf{c}) , predict what the *same* cell would look like if its concepts had been set to \mathbf{c}' instead.

Notation. We use capital letters for random variables (U, U_C, C, X) , lowercase bold for observed data $(\mathbf{x}, \mathbf{c}, \mathbf{c}')$, and lowercase with hats for model predictions $(\hat{\mathbf{c}}, \hat{\mathbf{u}})$.

Data-generating process. We adopt Pearl’s structural causal model (SCM) formalism (Pearl, 2009). A gene expression X is influenced by two sources of variation as illustrated in Figure 1: the observed concepts C and unobserved residual factors U . Concepts themselves are driven by their own exogenous variables U_C :

$$\begin{aligned} U &\sim P(U), & U_C &\sim P(U_C), \\ C &\leftarrow f_C(U_C), & X &\leftarrow f_X(C, U). \end{aligned} \quad (1)$$

where $P(U)$ and $P(U_C)$ are probability distributions over the unobserved factors, and f_C and f_X are functions that determine how these factors generate concepts and gene expression, respectively. We assume $U \perp U_C$; therefore $U \perp C$ under $C \leftarrow f_C(U_C)$.

Counterfactuals. The key insight is to ask “*what if*” questions about cells. Given observed gene expression \mathbf{x} and associated concepts \mathbf{c} , we ask: what would the *same* cell look like if its concepts were instead \mathbf{c}' , everything else being equal? We refer to the observed gene expression as the *factual* outcome X , and the hypothetical alternative as the *counterfactual* outcome X' . Formally, for a given unobserved residual factor \mathbf{u} , if the concepts were \mathbf{c}' rather than \mathbf{c} , the counterfactual gene expression would be:

$$X'(\mathbf{u}) = f_X(\mathbf{c}', \mathbf{u}), \quad (2)$$

where \mathbf{u} represents the same unobserved factors that generated the original cell. Given a factual observation \mathbf{x} , we define the *counterfactual edit* of that cell to concepts \mathbf{c}' as the expected counterfactual outcome:

$$\mu_{\mathbf{x}, \mathbf{c}'} := \mathbb{E}_U[f_X(\mathbf{c}', U) \mid X = \mathbf{x}]. \quad (3)$$

This represents what we expect that specific cell would look like on average if it had concepts \mathbf{c}' instead, where the expectation is over the posterior of U given $X = \mathbf{x}$ (abduction).

Cell editing as counterfactual prediction. We model single-cell editing as learning a predictor of counterfactual edit (Equation 3). Given an observed cell \mathbf{x} with concepts \mathbf{c} , the goal is to learn a function f_θ that generates the cell under alternative concepts \mathbf{c}' :

$$\hat{\mathbf{x}}' = f_\theta(\mathbf{x}, \mathbf{c}') \approx \mu_{\mathbf{x}, \mathbf{c}'}. \quad (4)$$

In other words, f_θ estimates how the same cell \mathbf{x} would appear if its concepts were \mathbf{c}' rather than \mathbf{c} ; this is equivalent to the cell editing task.

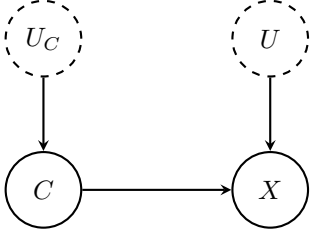


Figure 1. Directed Acyclic Graph (DAG) of the data-generating process. Two unobserved variables U and U_C drive X and C , respectively, with C also influencing X , consistent with $C \leftarrow f_C(U_C)$, $X \leftarrow f_X(C, U)$.

2.2. Architecture of scCBGM

The overall architecture of our model is shown in Figure 2. It follows an encoder–decoder design with a concept bottleneck. The encoder $E(\cdot)$ maps single-cell expression \mathbf{x} to a latent \mathbf{z} , which is decomposed into known factors $\hat{\mathbf{c}}$ and unknown factors \mathbf{u} reflecting the assumed data-generating process. These are concatenated and passed to the decoder $D(\cdot)$ to reconstruct \mathbf{x} . Details of the encoder, decoder, and bottleneck are given below, with losses and training described in Section 2.3.

Encoder The encoder $E(\cdot)$ is a neural network that maps an input $\mathbf{x} \in \mathbb{R}^d$ to the parameters of a multivariate Gaussian, defining the posterior distribution $q(\mathbf{z}|\mathbf{x}) = \mathcal{N}(\mu_z, \Sigma_z)$. A latent vector \mathbf{z} is then sampled from this distribution.

Concept bottleneck module The concept bottleneck module is composed of (1) a concept network (Koh et al., 2020) that parametrizes a function f_c mapping the latent representation \mathbf{z} into concept predictions $\hat{\mathbf{c}} = f_c(\mathbf{z}) \in \mathbb{R}^K$, and (2) a network f_u that produces representation $\mathbf{u} = f_u(\mathbf{z}) \in \mathbb{R}^{d_u}$ capturing variation not explained by $\hat{\mathbf{c}}$. We refer to $\hat{\mathbf{c}}$ and \mathbf{u} as the known and unknown factors, respectively.

Decoder with concept skip connections The decoder is a network $D(\cdot)$ that takes the concatenation of the known and unknown factors as input ($\mathbf{h}_0 = [\mathbf{u}, \hat{\mathbf{c}}]$). At each layer $\ell > 1$, we feed the previous hidden state concatenated with the known factors:

$$\begin{aligned} \mathbf{h}_1 &= D_1(\mathbf{h}_0), \quad \ell = 2, \dots, L, \\ \mathbf{h}_\ell &= D_\ell([\mathbf{h}_{\ell-1}, \hat{\mathbf{c}}]), \quad \hat{\mathbf{x}} = D_{\text{final}}(\mathbf{h}_L). \end{aligned} \quad (5)$$

Including $\hat{\mathbf{c}}$ at every layer enforces a stronger and more systematic conditioning on the concepts. This leads to better performance than only adding $\hat{\mathbf{c}}$ in the input \mathbf{h}_0 , especially when dealing with noisy concept annotations, as demonstrated empirically in Section 3.

2.3. Loss functions and training

We train the model by minimizing a loss derived from the β -VAE evidence lower bound (ELBO), *i.e.*, a reconstruc-

tion term, a concept supervision term, and a β -scaled KL regularization:

$$\begin{aligned} \mathcal{L}_{\text{VAE}} &= -\mathbb{E}_{q(\mathbf{z}|\mathbf{x})}[\log p(\mathbf{x}|\mathbf{z})] + \lambda_c \mathcal{L}_{\text{concept}} \\ &\quad + \beta \text{KL}(q(\mathbf{z}|\mathbf{x}) \parallel p(\mathbf{z})). \end{aligned} \quad (6)$$

where $\mathcal{L}_{\text{concept}}$ is a surrogate for $-\mathbb{E}_{q(\mathbf{z}|\mathbf{x})}[\log p(\mathbf{c}|\mathbf{z})]$, as described next.

Concept loss $\mathcal{L}_{\text{concept}}$ Biological data often has missing concept annotations. To accommodate this, we define a binary mask $\mathbf{m} \in \{0, 1\}^K$ indicating which of the K total concepts are present for a given sample. We partition the concepts into binary and continuous sets, indexed by K_{bin} and K_{cont} respectively. The total concept loss is the normalized sum of the **Binary Cross Entropy (BCE)** loss for binary concepts and the **Mean Squared Error (MSE)** loss for continuous concepts:

$$\begin{aligned} \mathcal{L}_{\text{concept}} &= \frac{1}{\sum_k m_k} \left(\sum_{k \in K_{\text{bin}}} m_k \mathcal{L}_{\text{BCE}}(\hat{c}_k, c_k) \right. \\ &\quad \left. + \sum_{k \in K_{\text{cont}}} m_k \mathcal{L}_{\text{MSE}}(\hat{c}_k, c_k) \right). \end{aligned} \quad (7)$$

where \hat{c}_k is the prediction for the ground-truth concept c_k .

Cross-covariance penalty To enforce independence between latent factors U and concepts C , we penalize their cross-covariance. Unlike cosine-similarity losses, this approach accommodates arbitrary embedding dimensions ($K \neq d_u$). For a minibatch of size B , the penalty is the squared Frobenius norm of the empirical cross-covariance between predicted concepts $\hat{C} \in \mathbb{R}^{B \times K}$ and unknown factors $U \in \mathbb{R}^{B \times d_u}$:

$$\mathcal{L}_{\text{cc}} = \left\| \frac{1}{B-1} (\hat{C} - \mathbf{1}\mu_{\hat{c}}^\top)^\top (U - \mathbf{1}\mu_u^\top) \right\|_F^2 \quad (8)$$

where $\mu_{\hat{c}}$ and μ_u are the column mean vectors of \hat{C} and U , respectively. Scaling is enforced implicitly for \hat{C} via the **Concept Loss**, and for U via a ReLU non-linearity. This prevents degenerate solutions where the unknown factors take on near-zero values. This pushes the model to encode non-concept specific sources of variation (e.g., batch, cell type) in \mathbf{u} , as theoretically analyzed in Appendix B.1 and empirically demonstrated in Appendix D.7.

Final loss

The complete training objective is obtained by combining \mathcal{L}_{VAE} and \mathcal{L}_{cc} :

$$\mathcal{L} = \mathcal{L}_{\text{VAE}} + \lambda_{\text{cc}} \mathcal{L}_{\text{cc}} \quad (9)$$

To further motivate our choice of model architecture and loss function, we provide proofs for the consistency of the counterfactual estimator learnt by minimizing \mathcal{L} in Appendix B.

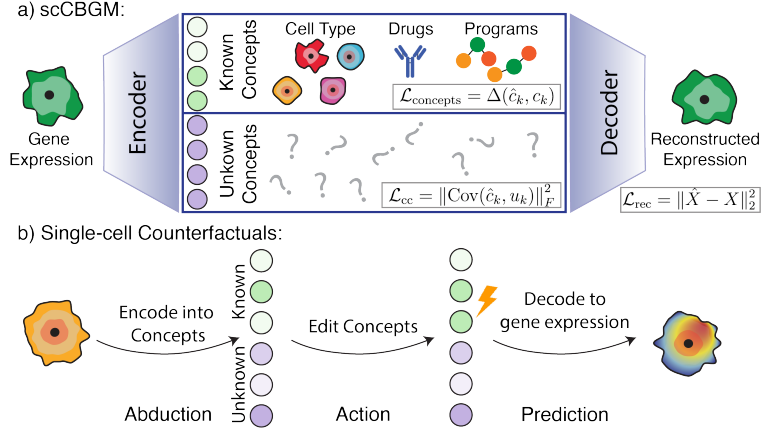


Figure 2. Single-cell Concept Bottleneck Generative Model Overview. **Top:** A concept bottleneck VAE encodes gene expression into known concepts and unknown concepts, which are subsequently decoded to reconstruct the expression profile. The model is trained to match the encoded concepts (\hat{c}_k) to the ground truth (c_k) while keeping the unknown concepts (u_k) independent via the cross-covariance loss. **Bottom:** Counter-factuals are constructed by: **1.** encoding each cells into its known and unknown concept. **2.** editing the desired concepts while keeping the rest stationary and **3.** decoding with the edited embedding.

Differences with standard concept bottleneck generative models. Our approach differs from standard CBGMs (Ismail et al., 2023) in three important ways: (i) we use a standard concept bottleneck model (Koh et al., 2020), where the bottleneck maps inputs to scalar concept predictions that directly correspond to interpretable concepts, rather than a concept embedding model (Espinosa Zarlenga et al., 2022) where the bottleneck maps each concept to high-dimensional representations;(ii) we add skip connections to the decoder to maintain persistent concept conditioning; and (iii) we use a cross-covariance loss (Mooij et al., 2009; Greenfeld & Shalit, 2020) instead of the cosine similarity loss for orthogonality. Changes (i) and (ii) improve robustness to noisy concept annotations, while change (iii) removes dimensional constraints on embeddings that are enforced by CBGMs. We show empirical performance gains compared to existing CBGMs in Section 3.

2.4. Counterfactual prediction

Our model enables counterfactual predictions by implementing the standard abduction-action-prediction framework (Pearl, 2009) with our generative architecture. **(1-Abduction Step)** Given an observed cell \mathbf{x} , we first encode it with our encoder to obtain $\mathbf{z} = E_\mu(\mathbf{x})$, and decompose it into concepts $\hat{\mathbf{c}}$ and unknown factors \mathbf{u} . **(2-Action Step)** We edit the desired concept values, to obtain a modified concept vector $\hat{\mathbf{c}}'$. We edit the vector $\hat{\mathbf{c}}$ by assigning the dimensions k for which the $\hat{\mathbf{c}}$ and $\hat{\mathbf{c}}'$ differ, and leave the other dimensions untouched. That is, $\hat{\mathbf{c}}' \equiv \hat{\mathbf{c}}_k \leftarrow \mathbf{c}'_k, \forall k : \mathbf{c}'_k \neq \mathbf{c}_k$. **(3-Prediction Step)** Lastly, we decode the modified representation $[\mathbf{u}, \hat{\mathbf{c}}']$ to produce the counterfactual prediction $\hat{\mathbf{x}}' = D([\mathbf{u}, \hat{\mathbf{c}}'])$. Figure 2 shows an illustration of the abduction-action-prediction process.

2.5. Enabling fine-grained control of generative models with scCBGM conditioning

While scCBGM is a standalone generative model, it can also enhance other generative models' architectures to enable more fine-grained control. By conditioning the generative process on the scCBGM embeddings, we can combine the generation quality of state-of-the-art generative models with the interpretability and controllability of our method. In this section, we describe the procedure for flow matching (FM) models (Lipman et al., 2023; Liu et al., 2023; Lipman et al., 2024); the extension to diffusion models is analogous.

scCBGM-guided FM Given a trained scCBGM-VAE, we train a flow matching model by directly conditioning on the scCBGM embeddings. For a cell \mathbf{x} , we extract its concept embeddings $\hat{\mathbf{c}} = f_c(\mathbf{z})$ and unknown representations $\mathbf{u} = f_u(\mathbf{z})$ where $\mathbf{z} = E_\mu(\mathbf{x})$. We use these vectors to learn a conditional vector field $v_\theta(\mathbf{x}_t, t; [\mathbf{u}, \hat{\mathbf{c}}])$ by minimizing the conditional flow matching loss:

$$\mathcal{L}_{\text{FM}} = \mathbb{E}_{t, \zeta \sim q, \mathbf{x}_t \sim p_t(\cdot | \zeta)} \left[\|v_\theta(\mathbf{x}_t, t; [\mathbf{u}, \hat{\mathbf{c}}]) - v^*(\mathbf{x}_t, t | \zeta)\|_2^2 \right]$$

Here, v^* is the target conditional velocity field that generates the conditional probability paths $p_t(\cdot | \zeta)$ for $t \in [0, 1]$, with $p_0(\cdot | \zeta)$ and $p_1(\cdot | \zeta)$ are boundary conditional probabilities whose marginal match with a noise distribution and the data distribution at $t = 0$ and $t = 1$ respectively (Lipman et al., 2023). The learnt conditional vector field $v_\theta(\mathbf{x}_t, t; [\mathbf{u}, \hat{\mathbf{c}}])$ generates a flow $\varphi_t(\mathbf{x}, [\mathbf{u}, \hat{\mathbf{c}}])$ defined by $\frac{d}{dt} \varphi_t(\mathbf{x}, [\mathbf{u}, \hat{\mathbf{c}}]) = v_\theta(\varphi_t(\mathbf{x}_t, [\mathbf{u}, \hat{\mathbf{c}}]), t; [\mathbf{u}, \hat{\mathbf{c}}])$ and $\varphi_0(\mathbf{x}, [\mathbf{u}, \hat{\mathbf{c}}]) = \mathbf{x}$. Using the flow, one can generate counterfactuals in two ways: decoding-only and encoding-decoding.

Decoding-only counterfactual prediction Given \mathbf{x} , we obtain $\hat{\mathbf{c}}'$ via the abduction and action steps on scCBGM. We

then predict the counterfactuals by sampling $\mathbf{x}_0 \sim \mathcal{N}(\mathbf{0}, \mathbf{I})$ and passing it to the conditional flow $\hat{\mathbf{x}}' = \varphi_1(\mathbf{x}_0, [\mathbf{u}, \hat{c}'])$. This approach is useful for generating diverse examples of cells with a specific profile. We refer to this approach as scCBGM-FM (decode).

Encoding-decoding counterfactual prediction A more accurate option for counterfactual prediction relies on mapping \mathbf{x} back to the noise distribution (encoding step) and then using the conditional flow from this initial condition to generate the modified cell (decoding step). Importantly, the encoding step uses a conditioning on \hat{c} while, the decoding uses the edited concepts \hat{c}' . Given a starting cell \mathbf{x} , we *encode* it using $\mathbf{x}_0 = \varphi_1^{-1}(\mathbf{x}, [\mathbf{u}, \hat{c}])$, then *decode* it using $\hat{\mathbf{x}}' = \varphi_1(\mathbf{x}_0, [\mathbf{u}, \hat{c}'])$. This implements Pearl’s abduction-action-prediction framework (Pearl, 2009; Xia et al., 2025; Rout et al., 2024): mapping \mathbf{x} to noise \mathbf{x}_0 constitutes the *abduction* of exogenous factors (cell identity), while the forward pass under intervention \hat{c}' performs the *action* and *prediction* (Sanchez & Tsafaris, 2022; Wang et al., 2024b). We refer to this approach as scCBGM-FM (edit).

3. Do we need a single-cell specific CBGM?

While concept bottleneck models have been explored in prior work, existing architectures do not address the unique challenges of scRNA-seq data, a modality that presents fundamentally different problems than well-curated domains such as images. In scRNA-seq, some concepts are well-defined by the experimental design (e.g., drug treatments, dosages), whereas others are inherently noisier (e.g., cell state, pathway activation). Noisy labels may arise from challenging annotation tasks, limited signal, incomplete coverage, or redundancy across concepts. To demonstrate that our architectural modifications address these challenges, we systematically compare scCBGM against standard CBGMs using synthetic data where ground-truth counterfactuals are available for direct evaluation.

Synthetic Data for Evaluation To compare model performance, we evaluate (1) cell-level counterfactual generation and (2) robustness to noisy concepts. Because real data do not permit controlled evaluation, we propose a synthetic scRNA-seq generation process based on a hierarchical overdispersed Poisson model (Pan et al., 2023; Xiao et al., 2021; Subedi & Dang, 2025). In this process, gene expression is decomposed into contributions from batches, tissues, cell types, and concepts. By isolating exogenous noise, we can generate true counterfactuals for evaluating model predictions. The process also supports the injection of four types of noisy concept annotations: incorrectly annotated, irrelevant, missing, and duplicated concepts. Appendix C.1-C.3 describes the data generating process, and Appendix C.4 details the noisy concept types.

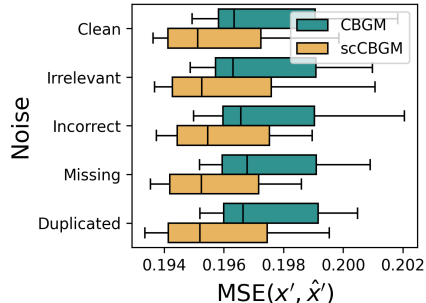


Figure 3. Standard CBGMs vs. scCBGM under different concept annotations noise. MSE between true and predicted counterfactuals across datasets (3), interventions (5), noise levels (3), and seeds (2).

Results We compare standard CBGMs with scCBGM to demonstrate the importance of our architectural modifications for single-cell data. Experiments use three synthetic datasets (20,000 cells, 5,000 genes) varying in technical noise and concept effect size (Appendix C.5). For each dataset, we hold out five concept–cell type pairs, meaning the model never observes these combinations during training, thus emulating a compositional generalization task (Appendix C.6). We evaluate robustness under four types of concept noise at two corruption levels with four random seeds. Intervention performance is measured by MSE between predicted and true counterfactuals. To ensure fairness, we conducted a hyperparameter sweep (432 configurations) on one noiseless dataset and selected the best model by intervention performance (Appendix C.7). Results are presented in Figure 3. scCBGM outperforms standard CBGM across all scenarios, both noisy and clean. scCBGM demonstrates greater robustness to noise, with only minimal performance degradation under different noise conditions. Furthermore, as shown in Appendix D.6, scCBGM remains stable as the number of concepts increases.

Ablation Study To evaluate the impact of our main architectural components, we conducted an ablation study varying three factors: the decoder type (skip vs. direct), the concept head (concept bottleneck vs. concept embedding), and the orthogonality loss (cross-covariance vs. cosine). Experiments were performed on three synthetic datasets, each with five intervention types, two random seeds, and multiple noise settings. The results, summarized in Table 15, indicate that the concept bottleneck (CBM) variant is preferable to the concept embedding (CEM) counterpart on this class of data. Within the CBM model family, incorporating the cross-covariance loss further improves performance. The skip-connection decoder enhances performance only when paired with both the cross-covariance loss and the concept-bottleneck architecture. This behavior is supported by ablations on real datasets, see Appendix D.8.2.

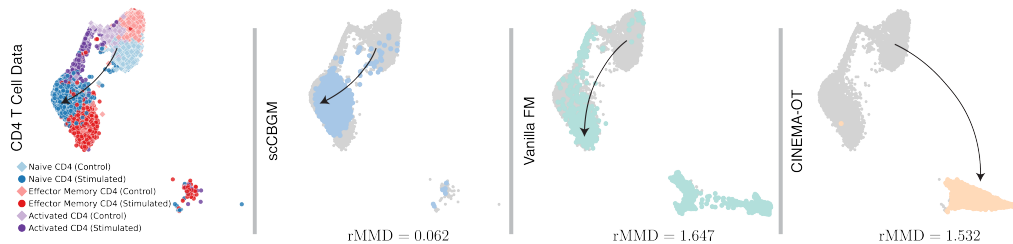


Figure 4. Counterfactual modeling predicts cellular response to perturbation. **Left:** UMAP of CD4 T-cell data from the Kang et al. data, showing Control and Stimulated cells, colored by subtype. Stimulated Naive CD4 T cells were held out during training. **Right:** Control Naive CD4 T cells are edited in silico to predict their stimulated state. scCBGM (second panel) accurately predicts the held-out stimulated Naive CD4 T cells, demonstrating superior zero-shot generalization compared to Vanilla-FM and CINEMA OT.

4. Related Works

scCBGM delivers accurate control over single-cell editing by uniquely integrating decoupled and interpretable representations with counterfactual generation. Existing methods typically address these aspects in isolation: most approaches for disentangled representations of single cells do not directly support interventions, while most intervention-based models capture conditional probability distributions without enabling fine-grained editing or counterfactual generation. Below, we review key methods from both domains.

Disentangled and interpretable representations for single cell data. Many methods have recently proposed interpretable latent decompositions for single cell data (Lopez et al., 2018; Svensson et al., 2020; Gut et al., 2021; Seninge et al., 2021; Choi et al., 2023; Lopez et al., 2023; Pouyabhar et al., 2025). Among these, a few combine interpretability with intervention prediction. For example, Celcomen (Megas et al., 2025) leverages disentangled representations to model gene–gene interactions in spatial data and MichiGAN (Yu & Welch, 2021) conditions a generative model on the latent space of a β -VAE which provides limited biological interpretability. Closer to our work, scDisInFac (Zhang et al., 2024) learns a disentangled representation of biological conditions and batch effects but assumes mutually independent factors and additive treatment mechanism in the latent space, which are unrealistic in our intended applications. biolord (Piran et al., 2024) incorporates interventions and use a noise injection mechanism for disentanglement. CinemaOT (Dong et al., 2023) first factors the data into causal and spurious factors before predicting treatment effects, but is limited to mapping cells to observations in the training data, restricting its generalizability.

Single-cell intervention prediction. scRNA-seq measurements cannot be repeated on the same cell, models typically predict intervention effects at the population level. Early approaches modeled temporal dynamics between cell populations (Yeo et al., 2021; Schiebinger et al., 2019), later extended to perturbation-response prediction (Rohbeck et al., 2025; Bunne et al., 2023; Klein et al., 2025).

Conditional generative models without explicit dynamics have also been adapted (Palma et al., 2025; Luo et al., 2024; Marouf et al., 2020; Huang et al., 2024). However, these models primarily learn *conditional distributions* and do not support counterfactual inference or cell-level editing. Moreover, many focus on specific perturbation classes such as gene knockouts (Roohani et al., 2023; Wang et al., 2024a; Littman et al., 2025) or chemical treatments (Qi et al., 2024), whereas our approach supports diverse biological interventions. Methods that attempt cell-level editing, such as scVIDR and scGen (Kana et al., 2023; Lotfollahi et al., 2019), depend on strong assumptions about perturbation mechanisms (e.g., additive latent effects) and do not provide interpretable representations.

5. Experiments

5.1. Experiment setup and metrics

We evaluate scCBGM on its ability to perform precise, fine-grained, and identity-preserving edits across three diverse real-world datasets (Kang et al., 2017; Cui et al., 2024; Nault et al., 2023). Since exogenous noise in real-world data cannot be controlled, exact counterfactual evaluation is infeasible. To approximate this, we treat broad cell-type categories as observable concepts (e.g., CD4 T cells) and consider granular subtypes (e.g., *activated* CD4 T cells) as ground-truth counterfactual distributions.

Let s denote a subtype. We define $\hat{p}_{s,c}$ as the empirical distribution of cells with subtype s under concept c . The corresponding ground-truth counterfactual distribution is $\hat{p}_{s,c'}$, i.e., the distribution of cells with the same subtype but different observable concept values. Since the subtype information is hidden from the model, it can be considered part of the exogenous noise U , making this construction a principled proxy for counterfactual evaluation.

Given a counterfactual predictor $f(x, c')$, we require the distribution induced by applying f to samples from $\hat{p}_{s,c}$ to align with $\hat{p}_{s,c'}$. We assess this alignment using the

Model	B cells	T cells (CD4)	T cells (CD8)	Monocytes (FCGR3A)	Monocytes (CD14)	Dendritic	NK cells
scCBGM	0.112 ± 0.028	0.169 ± 0.086	0.171 ± 0.012	1.845 ± 1.776	1.309 ± 0.231	0.375 ± 0.041	1.167 ± 0.271
scCBGM-FM (decode)	0.106 ± 0.032	0.162 ± 0.073	0.138 ± 0.040	1.141 ± 1.078	1.334 ± 0.296	0.288 ± 0.061	0.093 ± 0.016
scCBGM-FM (edit)	0.093 ± 0.031	0.156 ± 0.066	0.119 ± 0.019	1.206 ± 1.167	1.171 ± 0.390	0.231 ± 0.042	0.084 ± 0.003
CBGM	0.902 ± 0.058	2.228 ± 0.079	1.914 ± 0.049	9.514 ± 0.290	7.206 ± 0.196	1.503 ± 0.039	1.270 ± 0.140
Vanilla-FM(decode)	0.926 ± 0.067	1.037 ± 0.197	0.912 ± 0.079	4.389 ± 4.029	0.549 ± 0.240	2.250 ± 1.019	0.099 ± 0.015
Vanilla-FM(edit)	0.492 ± 0.174	0.487 ± 0.098	0.364 ± 0.078	2.188 ± 1.848	0.394 ± 0.095	1.307 ± 0.145	0.082 ± 0.021
biolord	2.622 ± 0.128	5.514 ± 1.856	4.829 ± 0.680	12.123 ± 11.118	2.350 ± 0.385	3.904 ± 1.480	2.355 ± 0.006
biolord-FM	1.163 ± 0.003	2.309 ± 0.003	1.762 ± 0.008	11.749 ± 0.054	10.091 ± 0.071	2.191 ± 0.010	1.051 ± 0.000
CINEMA-OT	2.259 ± 0.276	7.042 ± 2.520	5.362 ± 0.562	11.193 ± 9.807	10.185 ± 5.194	1.367 ± 0.333	3.707 ± 0.008
scGen	1.830 ± 0.397	5.117 ± 2.398	4.748 ± 0.072	7.227 ± 6.673	5.748 ± 0.349	1.133 ± 0.587	2.436 ± 0.072
CVAE	0.620 ± 0.008	1.374 ± 0.008	1.043 ± 0.027	9.055 ± 0.040	6.446 ± 0.067	1.134 ± 0.021	0.706 ± 0.010
CVAE-FM (decode)	0.525 ± 0.005	1.115 ± 0.010	0.901 ± 0.007	8.379 ± 0.045	6.051 ± 0.076	0.982 ± 0.012	0.604 ± 0.008
CVAE-FM (edit)	0.512 ± 0.003	1.080 ± 0.007	0.847 ± 0.005	8.442 ± 0.066	5.930 ± 0.067	0.987 ± 0.013	0.567 ± 0.004

Table 1. rMMD per cell group for different models (best, 2nd best, and 3rd best bolded) in the Kang et al. (2017) dataset.

Maximum Mean Discrepancy ratio (rMMD):

$$\text{rMMD} = \frac{\text{MMD}((f_{c'})\#\hat{p}_{s,c}, \hat{p}_{s,c'})}{\min_c \text{MMD}(\hat{p}_c, \hat{p}_{s,c'})}. \quad (10)$$

Here, $(f_{c'})\#\hat{p}_{s,c}$ denotes the distribution induced by transforming $\hat{p}_{s,c}$ with f , while \hat{p}_c is the empirical distribution of cells under concept c . The denominator minimizes MMD over all observed concepts in the training data, normalizing for baseline misspecification common in single-cell perturbation modeling (Wenteler et al., 2024). Intuitively, the numerator measures the discrepancy between predicted and observed counterfactuals at the subtype level, while the denominator reflects the similarity between the target population and its closest match in the training data. An rMMD below 1 indicates success, i.e., the model outperforms the trivial baseline of mapping to the most similar existing population. Analogously, we also evaluate the Frchet Inception Distance ratio and the Sinkhorn Divergence ratio, which are presented in Appendices D.2 and D.9.

Baselines. scCBGM is compared against CBGM, a standard concept bottleneck model (Ismail et al., 2023), as well as single-cell editing baselines: CINEMA-OT (Dong et al., 2023), biolord (Piran et al., 2024), scGen (Lotfollahi et al., 2019), and a standard Conditional Flow Matching model, representing state-of-the-art generative modeling in single-cell analysis (akin to the framework used in CellFlow Klein et al. (2025)). We refer to this baseline as *Vanilla-FM*. A standard Conditional VAE (CVAE), a common approach in batch correction tasks which achieve disentanglement by implicitly regressing out conditioning variables via the latent, is also included. Benchmarks are further extended to scCBGM combined with flow matching models (scCBGM-FM). To verify that scCBGM-FM’s performance stems from the structured scCBGM latent space rather than solely the generative capabilities of Flow Matching, CVAE-FM and biolord-FM are also evaluated. Finally, for Vanilla-FM, CVAE-FM and scCBGM-FM, two counterfactual strategies—*edit* and *decode*—are evaluated as detailed in Sec-

tion 2.5. While all baselines successfully regenerated the Kang et al. (2017) dataset, scCBGM and scCBGM-FM demonstrated superior accuracy in reconstructing cell identity (Figure 10). Complete data processing and model implementation details are provided in Appendix D.

5.2. Benchmarking single-cell editing

Counter-factual modeling predicts cellular response to perturbation We first benchmarked scCBGM on predicting treatment responses across 14 immune cell subtypes using the Kang et al. (2017) dataset, which contains Peripheral Blood Mononuclear Cells (PBMCs) with and without IFN- β stimulation. For each subtype, the stimulation response was treated as an independent benchmark across all models. The model’s concepts included 7 high-level cell types and a binary indicator for IFN- β stimulation. Table 1 shows that scCBGM-based edits accurately predict the stimulation response while preserving subtype identity, significantly outperforming existing conditional generation methods in counterfactual accuracy on 5 out of the 7 experiments. Additional metrics can be found in Appendix D.9. While Table 1 reports average rMMD across all CD4 T cell subtypes, Figure 4 illustrates this zero-shot generalization capability for a specific subtype. Here, we held out stimulated Naive CD4 T cells during training and evaluated our model’s ability to predict their response from control Naive CD4 T cells. We find that scCBGM accurately predicts the held-out stimulated Naive CD4 T cells, demonstrating superior zero-shot generalization compared to baseline methods.

The Cui et al. (2024) immune dictionary dataset measures the response of 17 immune cell subtypes across an expansive panel of 86 cytokine-based stimulations. This setting presents a more challenging scenario, requiring the model to learn distinct responses for each perturbation applied to different cell types. Concepts here included both broad cell type and stimulation identity. The counterfactual task was to predict the response of control cells to a particular stimulation, which the model had not encountered in com-

Model	Cui et al. (2024) dataset				Nault et al. (2023) dataset		
	T cells (Gamma-delta)	T cells (CD4)	T cells (CD8)	Dendritic (Langerhans)	Hepatocytes (Centrilobular)	Stellate cell	Hepatocytes (Periportal)
scCBGM	0.304 ± 0.024	0.062 ± 0.014	0.295 ± 0.038	0.110 ± 0.007	0.627 ± 0.011	0.895 ± 0.548	0.752 ± 0.046
scCBGM-FM (decode)	0.238 ± 0.032	0.046 ± 0.011	0.259 ± 0.042	0.104 ± 0.005	0.608 ± 0.029	0.861 ± 0.440	0.719 ± 0.056
scCBGM-FM (edit)	0.278 ± 0.017	0.034 ± 0.012	0.254 ± 0.022	0.097 ± 0.003	0.617 ± 0.001	0.844 ± 0.451	0.708 ± 0.056
CBGM	0.824 ± 0.151	0.401 ± 0.113	0.389 ± 0.054	0.139 ± 0.009	1.470 ± 0.695	0.979 ± 0.014	1.343 ± 0.466
Vanilla-FM(decode)	1.822 ± 0.264	1.647 ± 0.252	1.721 ± 0.232	1.609 ± 0.110	1.458 ± 0.690	10.481 ± 7.058	1.185 ± 0.484
Vanilla-FM(edit)	0.540 ± 0.116	0.164 ± 0.037	0.210 ± 0.062	0.368 ± 0.058	0.442 ± 0.088	7.235 ± 3.239	1.030 ± 0.317
biolord	2.848 ± 0.005	2.308 ± 0.006	1.934 ± 0.004	2.751 ± 0.003	/	44.340 ± 32.531	4.707 ± 2.031
CINEMA-OT	2.033 ± 0.004	1.532 ± 0.003	1.244 ± 0.004	1.504 ± 0.002	4.667 ± 1.598	45.570 ± 33.289	5.295 ± 1.363
scGen	2.069 ± 0.074	2.849 ± 0.134	1.506 ± 0.083	0.388 ± 0.013	2.214 ± 0.642	12.067 ± 9.021	2.389 ± 0.798
CVAE	0.300 ± 0.007	0.049 ± 0.006	0.238 ± 0.012	0.127 ± 0.003	1.842 ± 0.809	1.349 ± 0.281	1.554 ± 0.433
CVAE-FM (decode)	0.284 ± 0.006	0.043 ± 0.006	0.224 ± 0.006	0.121 ± 0.003	1.333 ± 0.585	0.882 ± 0.117	1.143 ± 0.263
CVAE-FM (edit)	0.292 ± 0.003	0.036 ± 0.010	0.232 ± 0.011	0.117 ± 0.001	1.337 ± 0.569	0.853 ± 0.171	1.131 ± 0.253

Table 2. rMMD per cell group for different models (best, 2nd best, and 3rd best bolded) in the Cui et al. (2024) and Nault et al. (2023).

combination with that specific cell subtype during training. We restricted our evaluation to four cell-type–cytokine pairs previously identified by (Cui et al., 2024) to induce a significant transcriptional shifts relative to controls. As reported in Table 2 (left), scCBGM successfully predicts accurate cellular responses for these unseen combinations.

Modeling continuous dose responses and hypothesis generation To assess whether scCBGM can model continuous responses, we used the Nault et al. (2023) dataset, which measures liver responses to varying dosages of TCDD, a toxic dioxin compound. In this setting, concepts consisted of broad cell type and treatment dosage. The counterfactual task was to predict gene expression profiles for intermediate dosages, given that high and low dosages of the test subtypes were withheld during training. As shown in Table 2 (right), scCBGM generally outperforms other methods, thereby helping to fill experimental gaps while supporting mechanistic hypothesis generation. Results on all available cell types are given in Appendix D.9.3.

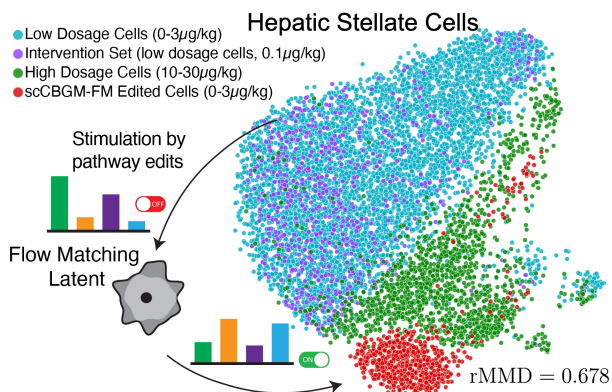


Figure 5. scCBGM enables interpretable control of cells to enhance response to stimulation. Stellate cells with low dosage of TCDD showed limited treatment response, while cells with high dosage showed a clear response. By editing control cells’ pathway activity, cells become more sensitive to TCDD, showing a treatment response similar to cells with higher TCDD dosage.

Benchmarking on synthetic data We benchmarked methods on the three synthetic datasets from Section 3, where access to true counterfactuals enables fine-grained cell-level rather than population-level evaluation. Flow matching models showed clear advantage, with scCBGM-FM outperforming all others across datasets (Appendix, Table 11).

scCBGM boosts performance of flow matching models. As discussed in Section 2.5, scCBGM can be combined with generative models to harness their established generative capabilities. Tables 1 and 2 compare scCBGM-FM directly with Vanilla-FM (*i.e.* our implementation of CellFlow). Whereas Vanilla-FM conditions the vector field only on observed concepts, allowing conditional but not fully counterfactual distributions, scCBGM-FM conditions on the scCBGM embedding, enabling richer counterfactual inference. In our experiments, scCBGM-FM improved over or matches vanilla-FM in 12/14 of the cell types across all datasets. We also note that the *edit* procedure is generally much more effective than the *decode* procedure. More broadly, the two components play complementary roles: base scCBGM provides the structured, disentangled latent space that enables interpretable concept-level editing, whereas scCBGM-FM (*edit*) leverages this representation for higher-fidelity generation. The reported gains therefore reflect the framework as a whole rather than either component in isolation.

5.3. Case study: controlled single-cell editing for enhanced drug response

Beyond cell-editing, we show that scCBGM offers a framework for guiding cells toward a desired biological state in an interpretable manner. In the original Nault et al. (2023) dataset, stellate cells exhibited only a moderate response to TCDD. With scCBGM, we can identify biological concepts that appear to be crucial for mediating the treatment effect in this specific cell type. To this end, we trained the model with gene regulation pathways extracted from a reference signaling pathway database (Badia-i Mompel et al.,

2022; Schubert et al., 2018), represented as soft concepts (*i.e.*, continuous values). By comparing control and treated stellate cells, we uncovered key pathways that were differentially regulated. We then applied scCBGM to edit control cells by jointly activating these pathways while simulating TCDD treatment. As illustrated in Figures 5, 14 & 15, the resulting cell population after editing appeared similar to the populations which responded to the treatment, in both rMMD and gene-expression changes. That is despite the model not being trained on any treatment data, suggesting a potential mechanistic route for mediating treatment response. These results highlight the utility of scCBGM for testing mechanistic hypotheses and exploring strategies to overcome cellular resistance.

6. Discussion and conclusion

We introduced scCBGM, a framework for interpretable and precise single-cell counterfactual editing. Our experiments demonstrate improved accuracy, flexibility, and robustness over existing methods, including under noisy annotations.

Limitations. Our evaluation approach involves assessing counterfactual methods on real single-cell data: true cell-specific counterfactuals cannot be observed, as this would require measuring the same cell under different conditions simultaneously. For real data, we therefore rely on population-level metrics as the best available approximation for validating cell-level edits. While this approach is standard in the field, it introduces a potential pitfall: population-level accuracy does not guarantee that individual cell predictions preserve biological realism or cell identity at the single-cell level. Our synthetic data evaluation addresses this limitation by providing access to ground-truth counterfactuals under controlled conditions. A further limitation concerns generalization scope: scCBGM generalizes to unseen combinations of known concepts but not to entirely new concepts absent from training, as each concept must be explicitly learned. However, this annotation bottleneck is partially mitigated by the fact that concepts can be learned in a semi-supervised manner, reducing the need for fully labeled data. Methods relying on a pretrained concept encoder (*e.g.*, biolord) can in principle accept novel concept embeddings at inference, reflecting a design tradeoff rather than a strict advantage. Extending scCBGM to novel concepts, *e.g.* via Label-Free CBMs (Oikarinen et al., 2023), is an interesting direction for future work.

Impact Statement

This work enables researchers to navigate combinatorial spaces of cellular responses that are experimentally infeasible to map, accelerating therapeutic design. However, high-fidelity generative models carry ethical risks, such as

the potential for fabricating biological data. Furthermore, an over-reliance on simulated counterfactuals without rigorous experimental validation could lead to false therapeutic leads, wasting critical resources.

References

- Adduri, A. K., Gautam, D., Bevilacqua, B., Imran, A., Shah, R., Naghipourfar, M., Teyssier, N., Ilango, R., Nagaraj, S., Dong, M., et al. Predicting cellular responses to perturbation across diverse contexts with state. *BioRxiv*, pp. 2025–06, 2025.
- Aevermann, B. D., Novotny, M., Bakken, T., Miller, J. A., Diehl, A. D., Osumi-Sutherland, D., Lasken, R. S., Lein, E. S., and Scheuermann, R. H. Cell type discovery using single-cell transcriptomics: implications for ontological representation. *Human Molecular Genetics*, 27(R1): R40–R47, 2018.
- Badia-i Mompel, P., Vélez Santiago, J., Braunger, J., Geiss, C., Dimitrov, D., Müller-Dott, S., Taus, P., Dugourd, A., Holland, C. H., Ramirez Flores, R. O., et al. decoupler: ensemble of computational methods to infer biological activities from omics data. *Bioinformatics advances*, 2 (1):vbac016, 2022.
- Bergen, V., Lange, M., Peidli, S., Wolf, F. A., and Theis, F. J. Generalizing RNA velocity to transient cell states through dynamical modeling. *Nature Biotechnology*, 38 (12):1408–1414, 2020. ISSN 1546-1696.
- Bunne, C., Stark, S. G., Gut, G., Del Castillo, J. S., Levesque, M., Lehmann, K.-V., Pelkmans, L., Krause, A., and Rätsch, G. Learning single-cell perturbation responses using neural optimal transport. *Nature methods*, 20(11):1759–1768, 2023.
- Chen, H., Lu, Y., Dai, Z., Yang, Y., Li, Q., and Rao, Y. Comprehensive single-cell RNA-seq analysis using deep interpretable generative modeling guided by biological hierarchy knowledge. *Briefings in Bioinformatics*, 25(4), 2024. URL <https://doi.org/10.1093/bib/bbae314>.
- Choi, Y., Li, R., and Quon, G. siVAE: interpretable deep generative models for single-cell transcriptomes. *Genome biology*, 24(1):29, 2023.
- Cui, A., Huang, T., Li, S., Ma, A., Pérez, J. L., Sander, C., Keskin, D. B., Wu, C. J., Fraenkel, E., and Hacohen, N. Dictionary of immune responses to cytokines at single-cell resolution. *Nature*, 625(7994):377–384, 2024.
- Dong, M., Wang, B., Wei, J., de O. Fonseca, A. H., Perry, C. J., Frey, A., Ouerghi, F., Foxman, E. F., Ishizuka, J. J.,

- Dhodapkar, R. M., et al. Causal identification of single-cell experimental perturbation effects with CINEMA-OT. *Nature methods*, 20(11):1769–1779, 2023.
- Espinosa Zarlenga, M., Barbiero, P., Ciravegna, G., Marra, G., Giannini, F., Diligenti, M., Shams, Z., Precioso, F., Melacci, S., Weller, A., et al. Concept embedding models: Beyond the accuracy-explainability trade-off. *Advances in Neural Information Processing Systems*, 35, 2022.
- Feydy, J., S ejourn e, T., Vialard, F.-X., Amari, S.-i., Trouv e, A., and Peyr e, G. Interpolating between optimal transport and mmd using sinkhorn divergences. In *The 22nd international conference on artificial intelligence and statistics*, pp. 2681–2690. PMLR, 2019.
- Greenfeld, D. and Shalit, U. Robust learning with the hilbertschmidt independence criterion. In *International Conference on Machine Learning*, pp. 3759–3768. PMLR, 2020.
- Gut, G., Stark, S. G., R atsch, G., and Davidson, N. R. Pm-VAE: Learning interpretable single-cell representations with pathway modules. *bioRxiv*, 2021.
- Huang, L., Xiong, L., Sun, N., Liu, Z., Wong, K.-C., and Kellis, M. A versatile informative diffusion model for single-cell atac-seq data generation and analysis. *Advances in Neural Information Processing Systems*, 37: 45462–45484, 2024.
- Ismail, A. A., Adebayo, J., Bravo, H. C., Ra, S., and Cho, K. Concept bottleneck generative models. In *International Conference on Learning Representations*, 2023.
- Ismail, A. A., Oikarinen, T., Wang, A., Adebayo, J., Stanton, S. D., Bravo, H. C., Cho, K., and Frey, N. C. Concept bottleneck language models for protein design. In *International Conference on Learning Representations*, 2025.
- Kana, O., Nault, R., Filipovic, D., Marri, D., Zacharewski, T., and Bhattacharya, S. Generative modeling of single-cell gene expression for dose-dependent chemical perturbations. *Patterns*, 4(8), 2023.
- Kang, H. M., Subramaniam, M., Targ, S., Nguyen, M., Maliskova, L., McCarthy, E., Wan, E., Wong, S., Byrnes, L., Lanata, C. M., Gate, R. E., Mostafavi, S., Marson, A., Zaitlen, N., Criswell, L. A., and Ye, C. J. Multiplexed droplet single-cell RNA-sequencing using natural genetic variation. *Nature Biotechnology*, 36(1):89–94, 2017.
- Klein, D., Fleck, J. S., Bobrovskiy, D., Zimmermann, L., Becker, S., Palma, A., Dony, L., Tejada-Lapuerta, A., Hugu et, G., Lin, H.-C., et al. Cellflow enables generative single-cell phenotype modeling with flow matching. *bioRxiv*, 2025.
- Koh, P. W., Nguyen, T., Tang, Y. S., Mussmann, S., Pierson, E., Kim, B., and Liang, P. Concept bottleneck models. In *International Conference on Machine Learning*, 2020.
- Korsunsky, I., Millard, N., Fan, J., Slowikowski, K., Zhang, F., Wei, K., Baglaenko, Y., Brenner, M., Loh, P.-r., and Raychaudhuri, S. Fast, sensitive and accurate integration of single-cell data with harmony. *Nature methods*, 16(12): 1289–1296, 2019.
- Lipman, Y., Chen, R. T., Ben-Hamu, H., Nickel, M., and Le, M. Flow matching for generative modeling. In *International Conference on Learning Representations*, 2023.
- Lipman, Y., Havasi, M., Holderrieth, P., Shaul, N., Le, M., Karrer, B., Chen, R. T., Lopez-Paz, D., Ben-Hamu, H., and Gat, I. Flow matching guide and code. *arXiv*, 2024.
- Littman, R., Levine, J., Maleki, S., Lee, Y., Ermakov, V., Qiu, L., Wu, A., Huang, K., Lopez, R., Scalia, G., et al. Gene-embedding-based prediction and functional evaluation of perturbation expression responses with presage. *bioRxiv*, 2025.
- Liu, X., Gong, C., et al. Flow straight and fast: Learning to generate and transfer data with rectified flow. In *The Eleventh International Conference on Learning Representations*, 2023.
- Lopez, R., Regier, J., Cole, M. B., Jordan, M. I., and Yosef, N. Deep generative modeling for single-cell transcriptomics. *Nature methods*, 15(12):1053–1058, 2018.
- Lopez, R., Tagasovska, N., Ra, S., Cho, K., Pritchard, J., and Regev, A. Learning causal representations of single cells via sparse mechanism shift modeling. In *Conference on Causal Learning and Reasoning*, pp. 662–691. PMLR, 2023.
- Lotfollahi, M., Wolf, F. A., and Theis, F. J. scGen predicts single-cell perturbation responses. *Nature methods*, 16(8):715–721, 2019.
- Luo, E., Hao, M., Wei, L., and Zhang, X. scdiffusion: conditional generation of high-quality single-cell data using diffusion model. *Bioinformatics*, 40(9), 2024.
- Marouf, M., Machart, P., Bansal, V., Kilian, C., Magruder, D. S., Krebs, C. F., and Bonn, S. Realistic in silico generation and augmentation of single-cell rna-seq data using generative adversarial networks. *Nature communications*, 11(1):166, 2020.
- Megas, S., Chen, D. G., Polanski, K., Eliasof, M., Sch onlieb, C.-B., and Teichmann, S. A. Estimation of single-cell and tissue perturbation effect in spatial transcriptomics via spatial causal disentanglement. In *International Conference on Learning Representations*, 2025.

- Mooij, J., Janzing, D., Peters, J., and Schölkopf, B. Regression by dependence minimization and its application to causal inference in additive noise models. In *Proceedings of the 26th annual international conference on machine learning*, pp. 745–752, 2009.
- Nault, R., Saha, S., Bhattacharya, S., Sinha, S., Maiti, T., and Zacharewski, T. Single-cell transcriptomics shows dose-dependent disruption of hepatic zonation by TCDD in mice. *Toxicological Sciences*, 191(1):135–148, 2023.
- Oikarinen, T., Das, S., Nguyen, L. M., and Weng, T.-W. Label-free concept bottleneck models. *arXiv preprint arXiv:2304.06129*, 2023.
- Palma, A., Richter, T., Zhang, H., Lubetzki, M., Tong, A., Dittadi, A., and Theis, F. J. Multi-modal and multi-attribute generation of single cells with CFGen. In *International Conference on Learning Representations*, 2025.
- Pan, Y., Landis, J. T., Moorad, R., Wu, D., Marron, J. S., and Dittmer, D. P. The poisson distribution model fits UMI-based single-cell RNA-sequencing data. *BMC Bioinformatics*, 24(1), 2023.
- Pearl, J. *Causality: Models, Reasoning and Inference*. Cambridge University Press, Cambridge, 2nd edition, 2009.
- Piran, Z., Cohen, N., Hoshen, Y., and Nitzan, M. Disentanglement of single-cell data with biolord. *Nature Biotechnology*, pp. 1–6, 2024.
- Pouyabahr, D., Andrews, T., and Bader, G. D. Interpretable single-cell factor decomposition using sciRED. *Nature communications*, 16(1):1878, 2025.
- Qi, X., Zhao, L., Tian, C., Li, Y., Chen, Z.-L., Huo, P., Chen, R., Liu, X., Wan, B., Yang, S., et al. Predicting transcriptional responses to novel chemical perturbations using deep generative model for drug discovery. *Nature Communications*, 15(1):1–19, 2024.
- Rohbeck, M., De Brouwer, E., Bunne, C., Huetter, J.-C., Biton, A., Chen, K. Y., Regev, A., and Lopez, R. Modeling complex system dynamics with flow matching across time and conditions. In *International Conference on Learning Representations*, 2025.
- Roohani, Y., Huang, K., and Leskovec, J. Predicting transcriptional outcomes of novel multigene perturbations with GEARS. *Nature Biotechnology*, 42(6):927–935, 2023.
- Rout, L., Chen, Y., Ruiz, N., Caramanis, C., Shakkottai, S., and Chu, W.-S. Semantic image inversion and editing using rectified stochastic differential equations. *arXiv preprint arXiv:2410.10792*, 2024.
- Sanchez, P. and Tsafaris, S. A. Diffusion causal models for counterfactual estimation. *arXiv preprint arXiv:2202.10166*, 2022.
- Schiebinger, G., Shu, J., Tabaka, M., Cleary, B., Subramanian, V., Solomon, A., Gould, J., Liu, S., Lin, S., Berube, P., Lee, L., Chen, J., Brumbaugh, J., Rigollet, P., Hochedlinger, K., Jaenisch, R., Regev, A., and Lander, E. S. Optimal-transport analysis of single-cell gene expression identifies developmental trajectories in reprogramming. *Cell*, 176(4):928–943.e22, 2019.
- Schubert, M., Klinger, B., Klünemann, M., Sieber, A., Uhlitz, F., Sauer, S., Garnett, M. J., Blüthgen, N., and Saez-Rodriguez, J. Perturbation-response genes reveal signaling footprints in cancer gene expression. *Nature communications*, 9(1):20, 2018.
- Senige, L., Anastopoulos, I., Ding, H., and Stuart, J. Vega is an interpretable generative model for inferring biological network activity in single-cell transcriptomics. *Nature communications*, 12(1):5684, 2021.
- Subedi, S. and Dang, U. J. Multivariate Poisson lognormal distribution for modeling counts from modern biological data: An overview. *Computational and Structural Biotechnology Journal*, 27:1255–1264, 2025.
- Svensson, V., Gayoso, A., Yosef, N., and Pachter, L. Interpretable factor models of single-cell RNA-seq via variational autoencoders. *Bioinformatics*, 36(11):3418–3421, 2020.
- Traag, V. A., Waltman, L., and Van Eck, N. J. From louvain to leiden: guaranteeing well-connected communities. *Scientific reports*, 9(1):1–12, 2019.
- Van der Vaart, A. W. *Asymptotic statistics*, volume 3. Cambridge university press, 2000.
- Wang, G., Liu, T., Zhao, J., Cheng, Y., and Zhao, H. Modeling and predicting single-cell multi-gene perturbation responses with scLAMBDA. *bioRxiv*, 2024a.
- Wang, J., Pu, J., Qi, Z., Guo, J., Ma, Y., Huang, N., Chen, Y., Li, X., and Shan, Y. Taming rectified flow for inversion and editing. *arXiv preprint arXiv:2411.04746*, 2024b.
- Wenteler, A., Occhetta, M., Branson, N., Huebner, M., Curean, V., Dee, W., Connell, W., Hawkins-Hooker, A., Chung, P., Ektefaie, Y., et al. Perteval-scfm: Benchmarking single-cell foundation models for perturbation effect prediction. *bioRxiv*, pp. 2024–10, 2024.
- Wolf, F. A., Angerer, P., and Theis, F. J. Scanpy: large-scale single-cell gene expression data analysis. *Genome biology*, 19(1):15, 2018.

- Wu, S. Z., Al-Eryani, G., Roden, D. L., Junankar, S., Harvey, K., Andersson, A., Thennavan, A., Wang, C., Torpy, J. R., Bartonicek, N., Wang, T., Larsson, L., Kaczorowski, D., Weisenfeld, N. I., Uytingco, C. R., Chew, J. G., Bent, Z. W., Chan, C.-L., Gnanasambandapillai, V., Dutertre, C.-A., Gluch, L., Hui, M. N., Beith, J., Parker, A., Robbins, E., Segara, D., Cooper, C., Mak, C., Chan, B., Warrior, S., Ginhoux, F., Millar, E., Powell, J. E., Williams, S. R., Liu, X. S., O’Toole, S., Lim, E., Lundeberg, J., Perou, C. M., and Swarbrick, A. A single-cell and spatially resolved atlas of human breast cancers. *Nature Genetics*, 53(9):1334–1347, 2021.
- Xia, T., Ribeiro, F. D. S., Rasal, R. R., Kori, A., Mehta, R., and Glocker, B. Decoupled classifier-free guidance for counterfactual diffusion models. *arXiv preprint arXiv:2506.14399*, 2025.
- Xiao, F., Tang, J., Fang, H., and Xi, R. Gene regulatory network in single cells based on the Poisson log-normal model, 2021.
- Yeo, G. H. T., Saksena, S. D., and Gifford, D. K. Generative modeling of single-cell time series with prescient enables prediction of cell trajectories with interventions. *Nature Communications*, 12(1), 2021.
- Yu, H. and Welch, J. D. Michigan: sampling from disentangled representations of single-cell data using generative adversarial networks. *Genome biology*, 22(1):158, 2021.
- Zhang, Z., Zhao, X., Bindra, M., Qiu, P., and Zhang, X. scdisinfact: disentangled learning for integration and prediction of multi-batch multi-condition single-cell RNA-sequencing data. *Nature Communications*, 15(1):912, 2024.
- Zhao, Y., Cai, H., Zhang, Z., Tang, J., and Li, Y. Learning interpretable cellular and gene signature embeddings from single-cell transcriptomic data. *Nature communications*, 12(1):5261, 2021.

Appendix

A. Additional details on Singe-Cell Concept Bottleneck Generative Models

A.1. A very short primer on counterfactuals

We posit a structural causal model (SCM) $M = (G, F, P(U))$ with a directed acyclic graph G , endogenous variables V , exogenous noise U , and assignments $F = \{v_i \leftarrow f_i(\text{pa}_i, u_i)\}$.

Intuitively, a counterfactual query asks: *What would an observed variable X have been, had we set a parent variable to a different value, while keeping everything else (including latent background U) fixed?*

Formally, counterfactuals are generated by applying the Pearlian do-operator within an SCM, and their values depend on both the structural assignments and the realization of U .

Setup in this paper. Let X denote a cell’s RNA-seq counts and C a concept variable we wish to intervene on. Let Z collect other endogenous covariates (e.g. other concepts). Then, we can abstract the data generating process as:

$$Z \leftarrow f_Z(\text{pa}_Z, U_Z), \quad (11)$$

$$C \leftarrow f_C(\text{pa}_C, U_C), \quad (12)$$

$$X \leftarrow f_X(Z, C, U_X). \quad (13)$$

Counterfactual of X under an action on C . For an observed cell with concept $C = c$, $X_{C=c} = x$, we write the counterfactual value of X if C had been set to c' as

$$X^{\text{cf}} = X_{\text{do}(C:=c')}(U), \quad (14)$$

defined by the standard abduction–action–prediction steps:

1. **Abduction:** infer the posterior $p(u, z \mid X_C = x)$ over latent variables;
2. **Action:** replace $C \leftarrow f_C(\cdot)$ by $C := c'$;
3. **Prediction:** compute $X^{\text{cf}} = f_X(z, c', u_X)$ with (z, u) drawn from the abducted posterior.

Given $X_{C=c} = x$, the probability distribution of the counterfactual is computed as follows:

$$p(x^{\text{cf}} \mid X_{C=c} = x, \text{do}(C := c')) = \int \mathbb{I}[f_X(z, c', u) = x^{\text{cf}}], p(z, u \mid X_{C=c} = x) dz du. \quad (15)$$

Ground-truth counterfactuals obtained from our synthetic data generating process When the data-generating process is fully known and simulatable, one can hold the exogenous noise U fixed and generate two outcomes with different concept values $C = c$ and $C = c'$. This yields

$$x = f_X(z, c, u_X), \quad (16)$$

$$x^{\text{cf}} = f_X(z, c', u_X), \quad (17)$$

for the same realization of (z, u_X) . Such pairs (x, x^{cf}) constitute *true counterfactual examples* and can serve as ground truth for evaluating predictive methods.

B. Consistency of our counterfactual predictor

In this Section, we prove the consistency of our counterfactual estimator. That is, in the infinite data regime, our estimator converges to the expected counterfactual outcome defined in Equation 3, as the following results shows.

Proposition B.1 (Consistency of scCBGMcounterfactuals). *Let $\hat{\theta}_n \in \arg \min_{\theta} \widehat{L}_n(\theta)$ be any empirical minimizer of the training objective in Equation 9 on n i.i.d. samples (\mathbf{x}, \mathbf{c}) . For \mathbf{x} fixed and any counterfactual edit \mathbf{c}' in the model's support, we define the learned counterfactual-mean predictor as*

$$g_{\theta}(\mathbf{x}, \mathbf{c}') := \mathbb{E}_{\mathbf{z} \sim q_{\theta}(\mathbf{z} | \mathbf{x})} [D_{\theta}([f_{u, \theta}(\mathbf{z}), \mathbf{c}'])]. \quad (18)$$

Assuming:

- (A1) (Data-generating SCM & exogeneity) $U \perp C$ with $X = f_X(C, U)$ and the target $\mu_{x, c'} := \mathbb{E}[f_X(\mathbf{c}', U) | X = \mathbf{x}]$ well-defined (exists and is finite).
- (A2) (Realizability) There exists θ^* such that the pushforward $(D_{\theta^*}([f_{u, \theta^*}(\mathbf{z}), \mathbf{c}]))_{\#} q_{\theta^*}(\mathbf{z} | \mathbf{x}) \equiv f_X(\mathbf{c}, U)_{\#} P(U | X = \mathbf{x})$, for all $\mathbf{c} \sim P(C)$.
- (A3) (Regularity) The parameter space is compact, The neural networks are bounded and Lipschitz in parameters and inputs. \widehat{L}_n admits near-global minimizers.
- (A4) (Uniform convergence) $\sup_{\theta} |\widehat{L}_n(\theta) - L(\theta)| \xrightarrow{P} 0$, where $L(\theta) = \mathbb{E}_{X, C}[\widehat{L}_n(\theta)]$
- (A5) (Support/positivity) \mathbf{c}' lies in the support of the training distribution of concepts (and in the support of the model).

We have:

$$g_{\hat{\theta}_n}(\mathbf{x}, \mathbf{c}') \xrightarrow{P} \mu_{x, c'}. \quad (19)$$

That is, the learned counterfactual mean converges in probability to the Pearlian counterfactual mean for the same cell \mathbf{x} under the edit \mathbf{c}' .

Proof Sketch. The proof follows an empirical minimization argument combined with the abduction-action-prediction formalism of counterfactual inference.

- (S1) From the consistency of M estimators (Van der Vaart, 2000), and assumption (A4), any sequence of empirical minimizers $\hat{\theta}_n$ converges in probability to $\theta^* := \arg \min_{\theta} L(\theta)$ (or to a set whose g_{θ} -image equals g_{θ^*}).
- (S2) At θ^* , (A2) leads $q_{\theta^*}(\mathbf{z} | \mathbf{x}) = p(\mathbf{z} | \mathbf{x})$ in the model's latent space and ensures $D_{\theta^*}([f_{u, \theta^*}(\mathbf{z}), \mathbf{c}])$ implements the true structural map $f_X(\mathbf{c}, U)$ when \mathbf{z} is drawn from that posterior.
- (S3) Let $T(\theta) := g_{\theta}(\mathbf{x}, \mathbf{c}')$. By (A3), we have that T is continuous at θ^* , so $T(\hat{\theta}_n) \xrightarrow{P} T(\theta^*)$.
- (S4) By (A2), the pushforward $(D_{\theta^*}([f_{u, \theta^*}(\mathbf{z}), \mathbf{c}]))_{\#} q_{\theta^*}(\mathbf{z} | \mathbf{x})$ matches $f_X(\mathbf{c}, U)_{\#} P(U | X = \mathbf{x})$. Hence,

$$T(\theta^*) = \int D_{\theta^*}([f_{u, \theta^*}(\mathbf{z}), \mathbf{c}']) q_{\theta^*}(\mathbf{z} | \mathbf{x}) dz = \int f_X(\mathbf{c}', \mathbf{u}) p(\mathbf{u} | \mathbf{x}) du = \mu_{x, c'}. \quad (20)$$

Combining (S3) and (S4), we have

$$g_{\hat{\theta}_n}(\mathbf{x}, \mathbf{c}') \xrightarrow{P} \mu_{x, c'}. \quad (21)$$

□

The realizability assumption is the crux of the above result. The following proposition shows that minimizing our loss in Equation 9 leads to the correct pushforward.

Proposition B.2 (Realizability of the pushforward). *Assume:*

- (A1) **SCM and exogeneity.** The data follow $X = f_X(C, U)$ with $U \perp C$, so that $f_X(\mathbf{c}, U)_{\#} P(U | X = \mathbf{x})$ is well-defined for all \mathbf{c}' .

- (A2) **Proper reconstruction and rich classes.** The reconstruction term in Equation 9 is a proper conditional risk for the law of X given the decoder input (e.g., a correctly specified exponential-family likelihood), and the encoder/decoder classes are rich enough to realize the data distribution. During training, the decoder is conditioned on the true c .
- (A3) **Concept supervision.** The concept head is consistent for predicting \mathbf{c} from \mathbf{x} under the chosen loss, so that at the population optimum we predict \mathbf{c} correctly.

Let $L(\theta)$ be the population objective corresponding to Equation 9, and let $\theta^* \in \arg \min_{\theta} L(\theta)$. Then for almost every \mathbf{x} and every \mathbf{c}' ,

$$(D_{\theta^*}([f_{u,\theta^*}(Z), \mathbf{c}']]) \#_{q_{\theta^*}}(Z | X = \mathbf{x})) = f_X(\mathbf{c}', U) \# P(U | X = \mathbf{x}), \quad (22)$$

i.e., the learned pushforward (decoder applied to the residual code with \mathbf{c}') matches the true counterfactual kernel in law. Equivalently, for any bounded measurable φ ,

$$\mathbb{E}[\varphi(D_{\theta^*}([f_{u,\theta^*}(Z), \mathbf{c}']]) | X = x)] = \mathbb{E}[\varphi(f_X(\mathbf{c}', U)) | X = \mathbf{x}]. \quad (23)$$

Proof sketch. (S1) (Optimal conditional reconstruction) From A2, because $-\log p_{\theta}(x | \mathbf{z}, \mathbf{c})$ is a strictly proper conditional scoring rule and the model class is rich, the population minimizer must realize the true conditional law of X given (Z, C) :

$$p_{\theta^*}(\mathbf{x} | Z, C) = p(\mathbf{x} | Z, C) \quad \text{a.s.} \quad (24)$$

Equivalently, there exists a measurable decoder D_{θ^*} such that $X = D_{\theta^*}([f_{u,\theta^*}(Z), C])$ almost surely under the joint law induced by (X, C) and $Z \sim q_{\theta^*}(\mathbf{z} | X)$.

- (S2) (Coupling with the structural SCM) Combine with Step 1: for a.s. (X, C) we can couple (Z, U) given $X=x$ so that

$$D_{\theta^*}([f_{u,\theta^*}(Z), C]) = f_X(C, U) \quad \text{a.s.}$$

This is just matching two a.s. representations of the same X under an appropriate coupling.

- (S3) (Kernel equality in law) Condition on $X = \mathbf{x}$ and replace C by any counterfactual value \mathbf{c}' . By the equality in Step 2 and the coupling of $(Z, U) | X = \mathbf{x}$, pushing $q_{\theta^*}(Z | X = \mathbf{x})$ through $\mathbf{u} \mapsto D_{\theta^*}([\mathbf{u}, \mathbf{c}'])$ yields the same law as pushing $P(U | X = \mathbf{x})$ through $u \mapsto f_X(\mathbf{c}', \mathbf{u})$:

$$(D_{\theta^*}([f_{u,\theta^*}(Z), \mathbf{c}']]) \#_{q_{\theta^*}}(Z | X = \mathbf{x})) = f_X(\mathbf{c}', U) \# P(U | X = \mathbf{x}), \quad \text{a.s.} \quad (25)$$

This is precisely the equality of the learned pushforward with the target counterfactual kernel. □

Note that Step 3 matches *measures on X* (the object we use for counterfactual prediction); it is invariant to internal reparameterizations of the residual code. The cross-cov penalty and independent training are used to *select* residuals \mathbf{u} that do not leak concept information, improving identifiability and stability.

B.1. Decoupling of known and unknown concepts through cross-covariance penalty

In Section 2.3 we introduced the cross-covariance loss \mathcal{L}_{cc} . Here we provide a theoretical proof for how the (predicted) known concepts $\hat{\mathbf{c}}$ and unknown factors \mathbf{u} become decoupled through the proposed loss. Let:

$$\mathbf{u} = \phi(A\mathbf{z} + \mathbf{a}^0), \quad \hat{\mathbf{c}} = \psi(B\mathbf{z} + \mathbf{b}^0) \quad (26)$$

where

$$A \in \mathbb{R}^{d_u \times d_z}, \quad B \in \mathbb{R}^{K \times d_z} \quad (27)$$

are weight matrices, and ϕ, ψ are element-wise, piecewise C^1 monotonically increasing activation functions (e.g., ReLU or sigmoid). The vectors $\mathbf{a}^0, \mathbf{b}^0$ are bias terms. We aim to show that using a cross-covariance loss

$$\mathcal{L}_{\text{cc}} = \|\text{Cov}(\mathbf{u}, \hat{\mathbf{c}})\|_F^2 \quad (28)$$

encourages decoupling between the representations \mathbf{u} and $\hat{\mathbf{c}}$. Define the Jacobians:

$$J_{\mathbf{u}}(\mathbf{z}) = \underbrace{\text{diag}(\phi'(A\mathbf{z} + \mathbf{a}^0))}_{D_{\mathbf{u}}} A, \quad J_{\hat{\mathbf{c}}}(\mathbf{z}) = \underbrace{\text{diag}(\psi'(B\mathbf{z} + \mathbf{b}^0))}_{D_{\hat{\mathbf{c}}}} B \quad (29)$$

We define the centered variables $\tilde{\mathbf{u}}$ and $\tilde{\hat{\mathbf{c}}}$ as:

$$\begin{aligned} \tilde{\mathbf{u}}(\mathbf{z}) &= \mathbf{u}(\mathbf{z}) - \mathbb{E}[\mathbf{u}(\mathbf{z})] \\ \tilde{\hat{\mathbf{c}}}(\mathbf{z}) &= \hat{\mathbf{c}}(\mathbf{z}) - \mathbb{E}[\hat{\mathbf{c}}(\mathbf{z})] \end{aligned} \quad (30)$$

If we assume that

$$\mathbb{E}[\mathbf{u}(\mathbf{z})] \approx \mathbf{u}(\mathbb{E}[\mathbf{z}]) \quad , \quad \mathbb{E}[\hat{\mathbf{c}}(\mathbf{z})] \approx \hat{\mathbf{c}}(\mathbb{E}[\mathbf{z}]) \quad (31)$$

Note: This assumption is true for all regions of the ReLU activation function where leakage is possible (positive domain).

Next, using a first order Taylor approximation we can linearize around $\boldsymbol{\mu}_{\mathbf{z}}$. Here, we define $\boldsymbol{\mu}_{\mathbf{x}} := \mathbb{E}[\mathbf{x}]$.

$$\tilde{\mathbf{u}}(\mathbf{z}) \approx \mathbf{u}(\mathbf{z}) - \underbrace{\mathbf{u}(\boldsymbol{\mu}_{\mathbf{z}})}_{\approx \boldsymbol{\mu}_{\mathbf{u}}} \approx J_{\mathbf{u}}(\boldsymbol{\mu}_{\mathbf{z}})(\mathbf{z} - \boldsymbol{\mu}_{\mathbf{z}}) \quad (32)$$

$$\tilde{\hat{\mathbf{c}}}(\mathbf{z}) \approx \hat{\mathbf{c}}(\mathbf{z}) - \underbrace{\hat{\mathbf{c}}(\boldsymbol{\mu}_{\mathbf{z}})}_{\approx \boldsymbol{\mu}_{\hat{\mathbf{c}}}} \approx J_{\hat{\mathbf{c}}}(\boldsymbol{\mu}_{\mathbf{z}})(\mathbf{z} - \boldsymbol{\mu}_{\mathbf{z}}) \quad (33)$$

With this we can express the covariance $\text{Cov}(\mathbf{u}, \hat{\mathbf{c}})$ as:

$$\text{Cov}(\mathbf{u}, \hat{\mathbf{c}}) = \mathbb{E}[\tilde{\mathbf{u}}\tilde{\hat{\mathbf{c}}}^T] \approx \mathbb{E}[J_{\mathbf{u}}(\boldsymbol{\mu}_{\mathbf{z}})(\mathbf{z} - \boldsymbol{\mu}_{\mathbf{z}})(\mathbf{z} - \boldsymbol{\mu}_{\mathbf{z}})^T J_{\hat{\mathbf{c}}}(\boldsymbol{\mu}_{\mathbf{z}})^T] \quad (34)$$

Which can be written as:

$$\text{Cov}(\mathbf{u}, \hat{\mathbf{c}}) \approx J_{\mathbf{u}}(\boldsymbol{\mu}_{\mathbf{z}})\Sigma_{\mathbf{z}}J_{\hat{\mathbf{c}}}(\boldsymbol{\mu}_{\mathbf{z}})^T, \quad \Sigma_{\mathbf{z}} := \text{Cov}(\mathbf{z}) \quad (35)$$

And thus minimizing the covariance means that:

$$\text{Cov}(\mathbf{u}, \hat{\mathbf{c}}) \rightarrow 0 \quad \Leftrightarrow \quad J_{\mathbf{u}}(\boldsymbol{\mu}_{\mathbf{z}})\Sigma_{\mathbf{z}}J_{\hat{\mathbf{c}}}(\boldsymbol{\mu}_{\mathbf{z}})^T \rightarrow 0 \quad (36)$$

Let us now look at what happens when we add some infinitesimal change $\delta\mathbf{z} \sim N(\mathbf{0}, \Sigma_{\mathbf{z}})$ around $\boldsymbol{\mu}_{\mathbf{z}}$:

$$\begin{aligned} \delta\mathbf{u} &= J_{\mathbf{u}}(\boldsymbol{\mu}_{\mathbf{z}})\delta\mathbf{z} \\ \delta\hat{\mathbf{c}} &= J_{\hat{\mathbf{c}}}(\boldsymbol{\mu}_{\mathbf{z}})\delta\mathbf{z} \end{aligned} \quad (37)$$

Then:

$$\text{Cov}(\delta\mathbf{u}, \delta\hat{\mathbf{c}}) = \mathbb{E}[\delta\mathbf{u}\delta\hat{\mathbf{c}}^T] = \mathbb{E}[J_{\mathbf{u}}(\boldsymbol{\mu}_{\mathbf{z}})\delta\mathbf{z}\delta\mathbf{z}^T J_{\hat{\mathbf{c}}}(\boldsymbol{\mu}_{\mathbf{z}})] \quad (38)$$

Which becomes:

$$\mathbb{E}[J_{\mathbf{u}}(\boldsymbol{\mu}_{\mathbf{z}})\delta\mathbf{z}\delta\mathbf{z}^T J_{\hat{\mathbf{c}}}(\boldsymbol{\mu}_{\mathbf{z}})] = J_{\mathbf{u}}(\boldsymbol{\mu}_{\mathbf{z}})\Sigma_{\mathbf{z}}J_{\hat{\mathbf{c}}}(\boldsymbol{\mu}_{\mathbf{z}}) = 0 \quad (39)$$

Hence, there's no first order covariance in the shift of \mathbf{u} and $\hat{\mathbf{c}}$ upon changes to \mathbf{z} along the direction of variance in the data. This concludes the proof that minimizing \mathcal{L}_{cc} enforces local decoupling between \mathbf{u} and $\hat{\mathbf{c}}$.

C. Synthetic data

C.1. Generative Process

Our synthetic data generation process builds on an overdispersed hierarchical Poisson distribution. For each cell i and gene j , the logarithm of the mean expression is modeled as the sum of several structured components. Because these factors are combined in log-space, their effects translate into multiplicative interactions on the original scale. Specifically, the log mean expression (λ_{ij}) is defined as:

$$\log(\lambda_{ij}) = w_j + l_j + \gamma_{b_{ij}} + \omega_{u_{ij}} + \tau_{t_{ij}} + \sum_{k=1}^K v_{ijk}c_{kj} + \varepsilon_{ij} \quad (40)$$

In this formulation, gene expression is decomposed into baseline levels (w_j), cell-specific scaling (l_i), batch effects ($\gamma_{b_{ij}}$), cell-type variation ($\omega_{u_{ij}}$), and tissue effects ($\tau_{t_{ij}}$). In addition, latent concept influences are captured by $\sum_{k=1}^K v_{ik} c_{kj}$, where v_{ik} denotes the activation of concept k in cell i , and c_{kj} its effect on gene j . Residual variation is represented by ε_{ij} . Gene expression counts are then sampled via the inverse transform method:

$$x_{ij} = Q(\delta_{ij}; \lambda_{ij}) = \inf\{k \in \mathbb{N} : F_{\text{Poi}}(k; \lambda_{ij}) > \delta_{ij}\}, \quad \delta_{ij} \sim \mathcal{U}(0, 1) \quad (41)$$

which is equivalent to drawing directly from the Poisson distribution:

$$x_{ij} \sim \text{Poi}(\lambda_{ij}) \quad (42)$$

Here, F_{Poi} denotes the cumulative distribution function (CDF) of the Poisson distribution, and Q its percent point function (PPF).

By explicitly modeling the exogenous noise (δ_{ij}), the framework enables the generation of true cell-level counterfactuals following concept-level interventions. To produce the counterfactual x'_{ij} , where we change concepts from c to c' , we simply do:

$$\begin{aligned} \log(\lambda'_{ij}) &= w_j + l_i + \gamma_{b_{ij}} + \omega_{u_{ij}} + \tau_{t_{ij}} + \sum_{k=1}^K v_{ik} \boxed{c'_{kj}} + \varepsilon_{ij} \\ x'_{ij} &= Q(\delta_{ij}; \lambda'_{ij}) \end{aligned} \quad (43)$$

The factors in the model are distributed as follows:

$l_i \sim \text{Norm}(0, \sigma_{b_{il}})$	(library size)
$\sigma_b \sim \text{Unif}(r_l, s_l)$	(library size std)
$w_j \sim \text{Unif}(r_w, s_w)$	(baseline expression)
$\varepsilon_{ij} \sim \text{Norm}(0, \sigma_\varepsilon)$	(noise)
$\gamma_{b_j} \sim \text{Norm}(0, \sigma_b)$	(batch effect)
$\tau_{t_j} \sim \text{Norm}(0, \sigma_t)$	(tissue effect)
$\omega_{u_j} \sim \text{Norm}(0, \sigma_u)$	(cell type effect)
$b_i \sim \text{Cat}(\mathbf{p}_i)$	(batch id)
$p_i \sim \text{Dir}(\alpha_b)$	(batch proportions)
$t_i \sim \text{Cat}(\mathbf{p}_q)$	(tissue id)
$p_q \sim \text{Dir}(\alpha_t)$	(tissue proportions)
$u_i \sim \text{Cat}(\mathbf{p}_{t_i})$	(cell type id)
$p_t \sim \text{Dir}(\alpha_u)$	(cell type proportions, in batch)

And the concept-related factors being:

$c_{kj} \sim \text{ZINorm}(\pi_k, 0, \sigma_c)$	(concept coefficient)
$\pi_k \sim \text{Beta}(\alpha, \beta)$	(zero inflation)
$p_u \sim \text{Dir}(\alpha_c)$	(concept probability, in cell type u)
$v_{ik} \sim \text{Ber}(p_{u_i k})$	(concept indicator)

Here we briefly describe the intuition behind the different terms:

- **library size** (l_i) – regulates the general expression level of cell i . This captures how some cells are more transcriptionally active than others.
- **baseline expression** (w_j) – the general expression level of gene j . This captures how some genes (e.g., housekeeping genes) tend to have similar expression across multiple cells.
- **batch id** (b_i) – the batch that cell i belongs to.

- **batch effect** (γ_{bj}) – how gene j is impacted in cells that belong to batch b . Batches can be, for example, different assays or collection sites.
- **tissue id** (t_i) – the tissue that cell i belongs to. The tissue distribution is dependent on the batch.
- **tissue effect** (τ_{tj}) – determines how gene j is impacted in cells that belong to tissue t . Tissue represents the anatomical region from which the sample was collected.
- **cell type id** (u_i) – the cell type that cell i belongs to. The tissue distribution is dependent on the batch. The cell type distribution is dependent on the tissue.
- **cell type effect** (ω_{uj}) – determines how gene j is impacted in cells that belong to tissue u . Cell type represents the phenotypic state of the cell.
- **concept activation** (v_{ik}) – the activation of concept k in cell i . In the synthetic data, the concepts are binary, hence $v_{ik} \in \{0, 1\}$. Concept activations are dependent on cell type, to mimic how the likelihood of a concept (e.g., biological pathways) being activated differs between cell types.
- **concept coefficients** (c_{kj}) – determines how concept k influences gene j . We model the concept coefficients with zero inflation to create a sparse concept coefficient matrix. This is similar to how most genes are not affected by a biological pathway being activated.

C.2. Motivation

scRNA-seq data is derived from a sequencing protocol in which cells are dissociated from tissue, their transcripts are barcoded, and the number of transcripts from each gene is counted. This process is inherently noisy: only a fraction of transcripts in each cell is captured and sequenced. As a result, modeling scRNA-seq data requires accounting for both measurement noise and biological variation.

Let x_{ij} denote the observed number of transcripts (i.e., gene count) for gene j in cell i , and let y_{ij} represent the true number of transcripts of gene j present in the cell prior to sequencing.

This process can be viewed as a random sampling step: a fixed number of transcripts n_i are captured from the full pool of $N_i = \sum_j y_{ij}$ transcripts present in cell i . Each captured transcript is barcoded and sequenced, resulting in observed counts x_{ij} .

The sampling is performed without replacement and can be modeled by a multivariate hypergeometric (MHG) distribution:

$$\mathbf{x}_i \sim \text{MHG}(\mathbf{t}_i, n_i) \quad (44)$$

where $\mathbf{t}_i = [t_{i1}, \dots, t_{iG}]$ denotes the true transcript counts per gene in cell i , and n_i is the total number of transcripts captured from that cell. The resulting vector \mathbf{x}_i describes how many transcripts of each gene were observed among the n_i sampled molecules.

Since only a small fraction of all transcripts are captured, we have:

$$\frac{\sum_j x_{ij}}{\sum_j y_{ij}} = \frac{n_i}{N_i} \rightarrow 0 \quad (45)$$

where $N_i = \sum_j y_{ij}$ is the true total number of transcripts. Under this low-sampling regime, the MHG distribution can be approximated by a multinomial distribution:

$$\mathbf{x}_i \sim \text{Multinomial}(n_i, \boldsymbol{\pi}_i), \quad \pi_{ij} = \frac{y_{ij}}{N_i} \quad (46)$$

Assuming that the total number of captured transcripts n_i follows a Poisson distribution with cell-specific rate η_i , we obtain:

$$P(\mathbf{x}_i = \mathbf{k}) = \text{Mult}(\mathbf{k} \mid n_i, \boldsymbol{\pi}_i) \text{Poi}(n_i \mid \eta_i) = \prod_j \text{Poi}(k_j \mid \eta_i \pi_{ij}) \quad (47)$$

Hence, the observed count for each gene j in cell i follows a Poisson distribution:

$$x_{ij} \sim \text{Poisson}(\eta_i \pi_{ij}) \quad (48)$$

This model captures measurement noise but assumes fixed proportions π_{ij} . In reality, gene expression varies across cells due to biological factors such as transcriptional bursting, regulation, or cell state heterogeneity. This leads to overdispersion in the observed counts:

$$\text{Var}(x_{ij}) > \mathbb{E}[x_{ij}]$$

To capture this variability, we treat the Poisson rate $\lambda_{ij} := \eta_i \pi_{ij}$ as a random variable, and model its logarithm as a sum of structured and stochastic components:

$$\begin{aligned} \log(\lambda_{ij}) &= w_j + l_i + \gamma_{b_{ij}} + \omega_{u_{ij}} + \tau_{t_{ij}} + \sum_{k=1}^{|C|} v_{ik} c_{kj} + \varepsilon_{ij} \\ x_{ij} &\sim \text{Poisson}(\lambda_{ij}) \end{aligned} \quad (49)$$

This formulation corresponds to a more general overdispersed Poisson model (e.g., a Poisson GLMM or latent variable model), which flexibly accounts for both technical and biological variability in scRNA-seq data.

C.3. Example of generated synthetic data

Figure 6 and Figure 7 show an example of synthetic data generated by our model, comprising 20,000 cells and 5,000 genes, with 2 batches, 2 tissue types, 4 cell types and 6 concepts. We let the effects from batch, tissue, cell type, and concepts follow the following impact order: batch > tissue > concept > cell type.

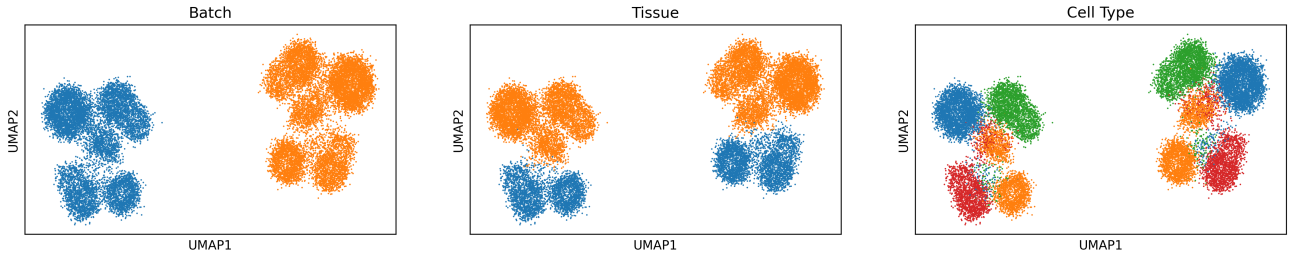


Figure 6. Example of synthetic data with highlighted covariates (batch, tissue, cell type). Each dot is a cell, coloring indicate is cells belonging to the same class (e.g, same batch or cell type). Class colors are subplot-specific and not comparable across panels.

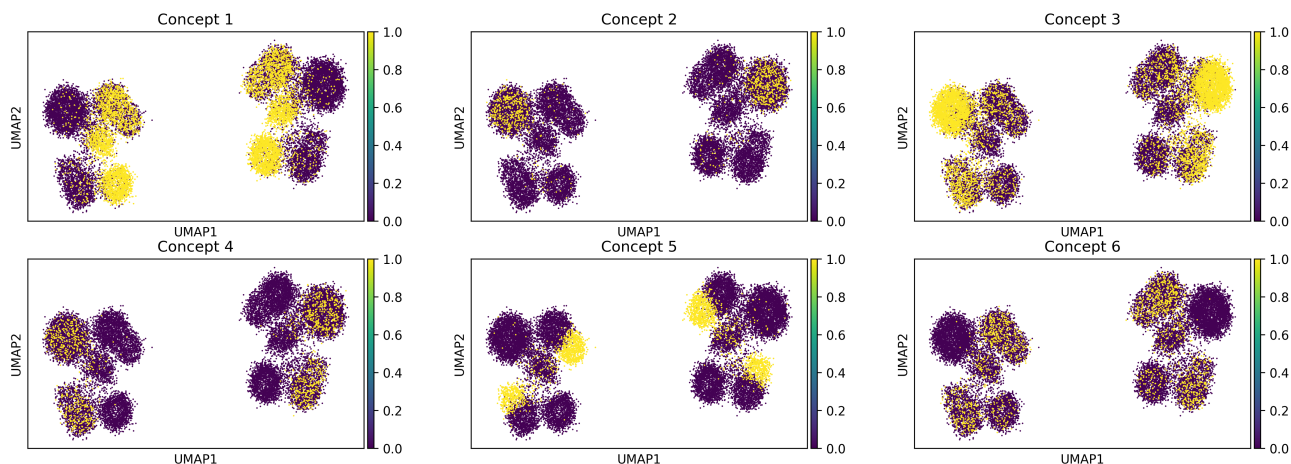


Figure 7. Same synthetic data as in Figure 6 but with highlighted concept activations. Each subplot correspond to one concept.

C.4. Noisy Concept Annotations

To evaluate robustness, we introduce controlled perturbations into the concept annotations, which we refer to as *noisy concepts*. These corruptions mimic realistic imperfections in annotation processes and take the following forms:

- **Missing:** Randomly removes a specified number or fraction of concept columns, simulating important concepts that are not annotated.
- **Irrelevant:** Adds concepts with random on/off values, emulating annotations that capture spurious or uninformative signals.
- **Incorrect:** Selects a subset of existing concepts and independently flips each entry ($0 \leftrightarrow 1$) with probability p_{noise} , mimicking systematic mislabeling at the concept level.
- **Duplicate:** Copies selected concept columns one or more times and appends them, increasing redundancy and inducing stronger—or potentially spurious—correlations between concepts and genes.

In all experiments, we evaluated two noise levels: corruption of 1 or 3 concepts. For the *Missing case*, this meant dropping 1 or 3 concepts; for *Irrelevant*, adding 1 or 3 artificial concepts; for *Incorrect*, randomly flipping a certain percentage of the values in 1 or 3 concepts; and for *Duplicate*, replicating 1 or 3 concepts. The intervened-upon concept was always left unaffected.

C.5. Synthetic Datasets

We generated three synthetic datasets with controlled variations in noise and concept effect strength. **Synthetic 1** serves as the baseline with default parameters. **Synthetic 2** increases "technical noise" ($\text{std_noise} = 0.08$), introducing more variability and reducing signal clarity. **Synthetic 3** reduces concept effect variance ($\text{std_concept} = 0.02$), producing sparser and weaker concept-driven influences on gene expression.

Dataset	std_noise	std_concept	Key difference vs. baseline
Synthetic 1	0.01	0.08	Baseline
Synthetic 2	0.08	0.08	More technical noise
Synthetic 3	0.01	0.02	Weaker concept effects

Table 3. Overview of synthetic datasets.

Shared parameters. All datasets were generated with **20,000 cells** and **5,000 genes**, across **4 cell types**, **3 tissues**, and **2 batches**, using **5 concepts**. Baseline expression values were sampled uniformly between 1 and 5, with batch, tissue, and cell type effects drawn from Normal distributions with standard deviations 0.06, 0.05, and 0.04, respectively. Library size variation was set between 0.01–0.03, residual noise at 0.01 (except where modified), and concept coefficients from a zero-inflated Normal with standard deviation 0.08 (except where modified). We let $\alpha = 1$, $\beta = 0.8$ in the Beta distribution used to sample π_k , impacting the sparsity of the genes that a concept influences.

C.6. Intervention Splits for Evaluation

For each dataset, we define 5 intervention tasks by holding out specific concept–cell type pairs, i.e., cases where a given concept is active in a particular cell type. The model is then asked to predict what cells of type u with the concept inactive would look like if it were switched on. This setup emulates a *compositional generalization* scenario. Concretely, let (u, k) denote a held-out pair, where u is the cell type and k the concept of interest:

- Remove all cells of type u with $c_k = 1$;
- Split all cells of type u with $c_k = 0$ into two equally sized groups: `train` and `intervene`
- Generate ground-truth counterfactuals for the `intervene` group using Eq. 43, yielding the `test` set
- Assign all remaining cells to the `train` group.

In this way, cells of type u are present in the training data, and cells with $c_k = 1$ are also present, but no instance of type u with $c_k = 1$ is ever observed during training. The model is trained on the `train` group, interventions are applied to the held-out `intervene` group, and predictions are evaluated against the corresponding counterfactuals in the `test` set. Because true counterfactuals are available for each intervened cell, evaluation can be performed at the cell level. The five intervention tasks are created by repeating this procedure across randomly chosen (u, k) pairs to ensure robust assessment.

C.7. Hyperparameter Sweep

For each model (scCBGM and CBGM) we performed a grid search over key hyperparameters. We use the dataset "Synthetic 1", with noiseless (clean) concept annotations for the sweep. Specifically, we varied the random seed $\{13, 69\}$, the latent dimension $\{64, 128\}$, hidden dimension $\{128, 256\}$, $\beta \in \{10^{-4}, 5 \times 10^{-5}, 10^{-5}\}$, learning rate $\{5 \times 10^{-4}, 10^{-5}\}$, orthogonality regularization $\{0.05, 0.2, 0.5\}$, and concept regularization $\{0.005, 0.05, 0.1\}$. Other parameters (e.g., bottleneck size = 128, 2 layers) were held fixed. We picked the set of hyperparameters that performed best across all five (synthetic interventions). This resulted in a total of 2160 different runs and a total of 432 hyperparameter sets that were evaluated. The full set of results across all sweeps are displayed in Figure 8.

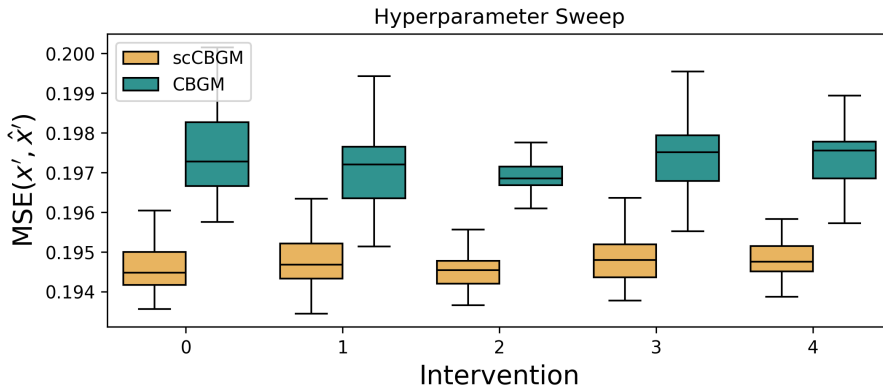


Figure 8. Results from hyperparameter sweep for the scCBGM and CBGM model. Error are cell-level MSEs, comparing the predicted counterfactual and the true counterfactual observation.

D. Experimental details

D.1. Data Processing

We benchmarked scCBGM and its Flow Matching variants against contemporary approaches for single-cell perturbations prediction on 3 datasets with annotated cell-types across varying perturbation conditions. Each dataset was minimally processed to fit within our counter-factual framework and to allow for systematic comparisons. The list of intervention variables for each dataset is given in Table 9.

D.1.1. KANG ET AL. PBMC IFN- β STIMULATION DATA

The (Kang et al., 2017) dataset comprises 24,264 cells across 8 broad-cell types, observed under two conditions: with and without IFN- β stimulation. We excluded megakaryocytes due to their low cell count (210 cells). Data was preprocessed using *scanpy* (Wolf et al., 2018), involving median library size normalization, log-transformation of all counts, and filtering to the top 3000 most highly expressed genes.

Table 4. Overview of cell types and subtypes with instance counts per condition. Note the sparsity in CD14+ Monocytes 1 (ctrl).

Broad	Subtype	Condition	Instances
B cells	B cells 0	ctrl	1105
	B cells 0	stim	1044
	B cells 1	ctrl	201
	B cells 1	stim	187
CD14+ Monocytes	CD14+ Monocytes 0	ctrl	2764
	CD14+ Monocytes 0	stim	2023
	CD14+ Monocytes 1	ctrl	9
	CD14+ Monocytes 1	stim	497
CD4 T cells	CD4 T cells 0	ctrl	2743
	CD4 T cells 0	stim	2743
	CD4 T cells 1	ctrl	1873
	CD4 T cells 1	stim	1830
	CD4 T cells 2	ctrl	538
	CD4 T cells 2	stim	518
CD8 T cells	CD8 T cells 0	ctrl	650
	CD8 T cells 0	stim	607
	CD8 T cells 1	ctrl	432
	CD8 T cells 1	stim	333
Dendritic cells	Dendritic cells 0	ctrl	159
	Dendritic cells 0	stim	126
	Dendritic cells 1	ctrl	44
	Dendritic cells 1	stim	98
FCGR3A+ Monocytes	FCGR3A+ Monocytes 0	ctrl	431
	FCGR3A+ Monocytes 0	stim	556
	FCGR3A+ Monocytes 1	ctrl	305
	FCGR3A+ Monocytes 1	stim	276
NK cells	NK cells 0	ctrl	915
	NK cells 0	stim	1047

Table 5. Overview of the cell types and subtypes in the (Kang et al., 2017) PBMC dataset.

To benchmark our model on high-fidelity edits that preserve cell phenotype while changing experimental conditions, we focused on identifying granular phenotypes consistent across stimulated and unstimulated cells. We first integrated the two conditions into a unified latent space using Harmony (Korsunsky et al., 2019). Within this unified latent space, we applied Leiden clustering (Traag et al., 2019) independently to each broad-cell type to discover direct subtypes. This process yielded a total of 14 subtypes, each approximately evenly distributed across the two experimental conditions, see Table 5. For the

Kang et al. (2017) experiments, concepts were defined using these original broad-cell types, while stimulation predictions and held-out validations were conducted at the more granular subtype level. We ran our experiments over the same 4 random seeds for all models. Table 6 presents the hyperparameters used for the Kang et al. (2017) experiments.

Table 6. Hyperparameters and seeds used in the Kang et al. (2017) experiments. All neural-network-based methods share `hidden_dim=1024`, `n_layers=4`, `batch_size=128`. For two-stage FM methods (biolord-FM, CVAE-FM, scCBM-FM), `Epochs` and `LR` refer to the FM training stage; the base model uses the same settings as its non-FM counterpart. β : KL divergence weight (`kl_hp` in ConceptFlow); z_{dim} : latent dimensionality; λ_{orth} : orthogonality regularisation weight. Dashes indicate not applicable. * Cinema-OT: `thresh=0.5`, `eps=0.001`. † biolord LRs: `latent_lr=decoder_lr=10-4`, `attribute_nn_lr=10-2`; penalty weights: `reconstruction_penalty=102`, `unknown_attribute_penalty=101`. ‡ biolord-FM FM component has `latent_dim=128` (independent of biolord’s `n_latent=32`). ConceptFlow additionally has `flow_hp=1.0`. § Ablation sweeps vary `use_cosine_loss` ∈ {T,F} and `decoder_type` ∈ {skip, no-residual, residual} (residual not included for CBGM). ¶ scCBM (no-var.) disables the variational bottleneck (`variational=False`), so there is no KL term and β does not apply.

Method	Data	Seeds	Epochs	LR	z_{dim}	β	<code>concepts_hp</code>	λ_{orth}	<code>model.edit</code>
scGen	kang	13, 42, 1337, 69	100	10^{-3}	—	—	—	—	—
CVAE	kang	13, 42, 1337, 69	200	3×10^{-4}	128	10^{-5}	—	—	—
scCBM	kang	13, 42, 1337, 69	200	3×10^{-4}	128	10^{-5}	0.1	0.5	—
CBGM	kang	13, 42, 1337, 69	200	3×10^{-4}	128	10^{-5}	0.1	0.5	—
biolord†	kang	13, 42, 1337, 69	100	10^{-4}	32	—	—	—	—
Cinema-OT*	kang	13, 42, 1337, 69	—	—	—	—	—	—	—
ConceptFlow	kang	13, 42, 1337, 69	200	3×10^{-4}	128	0.1	0.1	0.1	—
biolord-FM‡	kang	13, 42, 1337, 69	200	3×10^{-4}	128	—	—	—	—
CVAE-FM	kang	13, 42, 1337, 69	200	3×10^{-4}	128	10^{-5}	—	—	{edit, decode}
Vanilla-FM	kang	13, 42, 1337, 69	200	3×10^{-4}	128	—	—	—	{edit, decode}
scCBM-FM	kang	13, 42, 1337, 69	200	3×10^{-4}	128	10^{-5}	0.1	0.5	{edit, decode}
scCBM (abl.)§	kang	13, 42, 1337, 69	200	3×10^{-4}	128	10^{-5}	0.1	{0.0, 0.5}	—
CBGM (abl.)§	kang	13, 42, 1337, 69	200	3×10^{-4}	128	10^{-5}	0.1	{0.0, 0.5}	—
scCBM (no-var.)¶	kang	13, 42, 1337, 69	200	3×10^{-4}	128	—	0.1	0.5	—

D.1.2. CUI ET AL. IMMUNE DICTIONARY DATA

We further evaluated scCBGM using the Immune Dictionary dataset by (Cui et al., 2024). This dataset comprises 110,378 cells, encompassing over 17 distinct immune cell types stimulated with 86 different cytokines in vivo, providing a rich map of cellular responses to immune perturbations. For preprocessing, similar to the Kang et al. dataset, we applied median library size normalization, log-transformation of counts, and filtered to the top 3000 most highly expressed genes.

Unlike the Kang et al. data where we derived subtypes, the Cui et al. dataset already provides 17 granular immune cell type labels. For this dataset, we created broader concept groupings by pooling these original labels into seven aggregate cell types: Stromal cells, Granulocytes, Monocyte-Macrophages (referred to as myeloid in the tables), Dendritic cells, Innate lymphoid cells (referred to as lymphoid in the tables), B cells, and T cells. These broader categories served as our primary cell type concepts. Additionally, concepts were created for each cytokine stimulation. Consistent with our approach for the Kang et al. data, stimulation predictions and held-out validations were performed at the original, granular 17-subtype level.

Given the vast number of possible cytokine-cell type combinations (86 cytokines across 17 cell types), we focused our evaluation on a select set of seven cell-type - cytokine pairs. These pairs were chosen based on the Immune Dictionary paper’s findings, representing combinations shown to induce a significant transcriptional shift compared to control conditions. The specific intervention pairs evaluated were (cell type - cytokine):

- $\gamma\delta$ T cells - IL17E
- CD4 T cells - TGF β
- CD8 T cells - TNF α
- Conventional dendritic cells (cDC) 2 - INF α 1
- Langerhans - IFN γ

- Macrophages - M-CSF
- NK cells - IL15

We ran our experiments over the same 4 random seeds for all models. Table 7 presents the hyperparameters used for the Cui et al. (2024) experiments.

Table 7. Hyperparameters and seeds used in the Cui et al. (2024) experiments. All neural-network-based methods share `hidden_dim=1024`, `n_layers=4`, `batch_size=128`. For two-stage FM methods (biolord-FM, CVAE-FM, scCBM-FM), `Epochs` and `LR` refer to the FM training stage; the base model uses the same settings as its non-FM counterpart. β : KL divergence weight (`kl_hp` in ConceptFlow); z_{dim} : latent dimensionality of the learned representation or FM flow space; λ_{orth} : orthogonality regularization weight. Dashes indicate not applicable. * Cinema-OT is a non-parametric optimal-transport method; its only hyperparameters are `thresh=0.5` and `eps=0.001`. † biolord uses component-wise LRs: `latent_lr=decoder_lr=10-4`, `attribute_nn_lr=10-2`; additional loss weights: `reconstruction_penalty=102`, `unknown_attribute_penalty=101`. ‡ biolord-FM’s FM component has `latent_dim=128` (independent of biolord’s `n_latent=32`). ConceptFlow additionally has `flow_hp=1.0` (FM loss weight).

Method	Data	Seeds	Epochs	LR	z_{dim}	β	<code>concepts_hp</code>	λ_{orth}	<code>model.edit</code>
scGen	cui	13, 42, 1337, 69	100	10^{-5}	—	—	—	—	—
CVAE	cui	13, 42, 1337, 69	200	3×10^{-4}	128	10^{-5}	—	—	—
scCBM	cui	13, 42, 1337, 69	200	3×10^{-4}	128	10^{-5}	0.1	0.5	—
CBGM	cui	13, 42, 1337, 69	200	3×10^{-4}	128	10^{-5}	0.1	0.5	—
biolord [†]	cui	13, 42, 1337, 69	100	10^{-4}	32	—	—	—	—
Cinema-OT*	cui	13, 42, 1337, 69	—	—	—	—	—	—	—
ConceptFlow	cui	13, 42, 1337, 69	200	3×10^{-4}	128	0.1	0.1	0.1	—
biolord-FM ^{†‡}	cui	13, 42, 1337, 69	200	3×10^{-4}	128	—	—	—	—
CVAE-FM	cui	13, 42, 1337, 69	200	3×10^{-4}	128	10^{-5}	—	—	{edit, decode}
Vanilla-FM	cui	13, 42, 1337, 69	200	3×10^{-4}	128	—	—	—	{edit, decode}
scCBM-FM	cui	13, 42, 1337, 69	200	3×10^{-4}	128	10^{-5}	0.1	0.5	{edit, decode}

D.1.3. NAULT ET AL. LIVER DOSAGES RESPONSE DATASET

To assess scCBGM’s capacity for modeling continuous responses and its utility in cellular control, we utilized the Nault et al. dataset (Nault et al., 2023). This dataset comprises 131,613 cells across 11 granular cell types of liver responses to varying dosages of TCDD, a toxic dioxin compound, ranging from $0\mu\text{g}/\text{kg}$ up to $30\mu\text{g}/\text{kg}$. Preprocessing followed the same procedure as the other datasets: median library size normalization, log-transformation of counts, and filtering to the top 3000 most highly expressed genes.

We conducted two primary experiments using this dataset:

Continuous Dosage Prediction For this experiment, concepts were defined to include broad cell types and TCDD dosage. The 11 original cell types were grouped into four broad categories: Hepatocyte, Immune cells, Cholangiocyte, and Stromal, which served as hard concepts. TCDD dosage was treated as a soft (continuous) concept and its true values were log-transformed and then scaled to be between 0 and 1. The counterfactual task involved predicting gene expression profiles for intermediate TCDD dosages, specifically holding out the 3 and $10\mu\text{g}/\text{kg}$ dosed test cell subtypes during training. This setup enabled benchmarking scCBGM’s ability to fill experimental gaps by inferring responses at unobserved dosage levels. For this experiment, we used a single seed and aggregated the results over the different treatment dosages.

Interpretable Cellular Control via Pathway Activation This experiment demonstrated scCBGM’s application in controlling cells towards a desired biological state, particularly enhancing treatment effects in specific cell types. We focused on hepatic stellate cells, which showed only a moderate response to TCDD in the original dataset (i.e., minimal effect at lower dosages, unlike hepatocytes, but responding at 10 and $30\mu\text{g}/\text{kg}$).

First, we computed gene-set loadings for PROGENy pathways (Schubert et al., 2018) using the *decoupler* package (Badia-i Mompel et al., 2022). By comparing responder hepatic stellate cells (dosed at 10 and $30\mu\text{g}/\text{kg}$) with non-responders (all other dosages), we identified differentially regulated pathways. Specifically, responder stellate cells exhibited high activity

in $TGF\beta$, PI3K, and p53 pathways, and low activity in Trail and VEGF pathways. All 15 PROGENy pathways were mapped to continuous concepts, with their values min-max scaled between 0 and 1 across the entire dataset.

For the editing task, all responder hepatic stellate cells were explicitly removed from the training data, meaning the model was unaware that these cells could respond to TCDD. We then performed in silico stimulation on control stellate cells by jointly modifying the soft concepts corresponding to the identified pathways (increasing $TGF\beta$, PI3K, p53, and decreasing Trail, VEGF), while simultaneously activating the TCDD dosage concept. Specifically, we intervened on hepatic stellate cells with a dosage of $0.01\mu\text{g}/\text{kg}$. We encoded these cells, edited their dose concept to $30\mu\text{g}/\text{kg}$, and shifted their $TGF\beta$, PI3K, p53, Trail, and VEGF pathway concepts to 0.598, 0.521, 0.327, 0.697, and 0.333 (respectively). These specific concept values represent the mean activations within the responder population.

The resulting edited cell population displayed markedly increased sensitivity to the compound, validating scCBGM’s ability to identify and modulate mechanistic routes for treatment response.

We used a single seed for all models and the standard deviations were obtained using the variability over different treatment dosages. Table 8 presents the hyperparameters used for the Nault et al. (2023) experiments

Table 8. Hyperparameters used in the Nault et al. (2023) experiments. All experiments use a single random seed (0). All neural-network-based methods share `hidden_dim=1024`, `n_layers=4`, `batch_size=128`. β : KL divergence weight; z_{dim} : latent dimensionality; λ_{orth} : orthogonality regularization weight. For two-stage FM methods (CB-FM, cVAE-FM), *Epochs* and *LR* refer to the FM training stage; the base model (scCBGM or CVAE) uses the same settings as its non-FM counterpart. The *inference mode* column distinguishes edit-mode (∇ -guided flow editing) from guided-mode (conditional decoding), corresponding to `edit=True/False` in the scripts; these are denoted *edit* and *guided* respectively (cf. *decode* in the CUI/Kang tables). Dashes indicate not applicable. * Cinema-OT: `thresh=0.5`, `eps=0.001`. † biolord LRs: `latent_lr=decoder_lr=10-4`, `attribute_nn_lr=10-2`; penalty weights: `reconstruction_penalty=102`, `unknown_attribute_penalty=101`. ‡ CBGM in the baselines script uses CEM.MetaTrainer with `max_epochs=200`; scCBGM in the main script uses CB.VAE.MIXED with `num_epochs=100`. Both share the same architectural hyperparameters.

Method	Seed	Epochs	LR	z_{dim}	β	concepts_hp	λ_{orth}	Inference mode
Cinema-OT*	0	—	—	—	—	—	—	—
scGen	0	100	10^{-5}	—	—	—	—	—
CBGM‡	0	200	3×10^{-4}	128	10^{-5}	0.1	0.5	—
biolord†	0	100	10^{-4}	32	—	—	—	—
scCBGM‡	0	100	3×10^{-4}	128	10^{-5}	0.1	0.5	—
CVAE	0	100	3×10^{-4}	128	10^{-5}	—	—	—
CB-FM	0	100	3×10^{-4}	128	—	—	—	{edit, guided}
Raw-FM	0	100	3×10^{-4}	128	—	—	—	{edit, guided}
cVAE-FM	0	100	3×10^{-4}	128	—	—	—	{edit, guided}

Table 9. Intervention variables used across the three datasets. # tasks counts the number of held-out (cell type, perturbation) conditions evaluated per dataset: for Kang et al. (2017) the same IFN- β stimulus is applied to multiple donor-cluster splits of each cell type, giving 14 tasks over 7 cell-type groups; for Nault et al. (2023) each cell type is evaluated at two held-out dose levels, giving 6 tasks over 3 cell types. All concepts are binary (0/1) or continuous (dose) scalars embedded in the concept bottleneck.

Dataset	Cell type	Perturbation	Reference state	Target state	# tasks
Cui et al. (2024)	CD4 T cells	TGF- β	PBS	TGF- β	1
	CD8 T cells	TNF α	PBS	TNF α	1
	$\gamma\delta$ T cells	IL-17E	PBS	IL-17E	1
	NK cells	IL-15	PBS	IL-15	1
	Macrophages	M-CSF	PBS	M-CSF	1
	cDC2	IFN α 1	PBS	IFN α 1	1
	Langerhans cells	IFN γ	PBS	IFN γ	1
Kang et al. (2017)	B cells	IFN- β	ctrl	stim	2
	CD4 T cells	IFN- β	ctrl	stim	3
	CD8 T cells	IFN- β	ctrl	stim	2
	CD14 ⁺ Monocytes	IFN- β	ctrl	stim	2
	Dendritic cells	IFN- β	ctrl	stim	2
	FCGR3A ⁺ Monocytes	IFN- β	ctrl	stim	2
	NK cells	IFN- β	ctrl	stim	1
Nault et al. (2023)	B cells	Drug dose	1.0	{3.0, 10.0}	2
	Macrophages	Drug dose	1.0	{3.0, 10.0}	2
	T cells	Drug dose	1.0	{3.0, 10.0}	2
Total					27

D.2. Evaluation metrics

We compare performance of different models using the following metrics: the Maximum Mean Discrepancy ratio (rMMD), the Fréchet Inception Distance ratio (rFID), and the Sinkhorn Divergence ratio (rSD). We give a definition of these metrics below. Complete benchmarking results with these metrics are provided in Appendix D.9.

Notations We define \hat{p}_c^* as the true empirical distribution of an initial cell population of interest with concept c , \hat{p}_c for the empirical distribution of the population of *all* cells with with concept c , $\hat{p}_{c \rightarrow c'}^*$ the distribution of the target counterfactual cell population of interest with concept c' . We write $\hat{p}_{c \rightarrow c'}$ for the *predicted* counterfactual distribution.

The ratio formulation normalizes the performance of the model’s prediction against the best achievable (lowest) metric among all cell populations, providing a scale-independent measure of relative quality.

rMMD The Maximum Mean Discrepancy ratio is defined as

$$\text{rMMD} = \frac{\text{MMD}(\hat{p}_{c \rightarrow c'}^*, \hat{p}_{c \rightarrow c'})}{\min_{\gamma} \text{MMD}(\hat{p}_{\gamma}, \hat{p}_{c \rightarrow c'}^*)}. \quad (50)$$

where rMMD is defined as the *squared* maximum mean discrepancy with kernel k :

$$\text{MMD}(p, q) = \mathbb{E}_p[k(X, X)] - 2\mathbb{E}_{p, q}[k(X, Y)] + \mathbb{E}_q[k(Y, Y)]. \quad (51)$$

In our experiments, we used the RBF kernel.

rFID The Fréchet Inception Distance ratio (rFID) is defined as

$$\text{rFID} = \frac{\text{FID}(\hat{p}_{c \rightarrow c'}^*, \hat{p}_{c \rightarrow c'})}{\min_{\gamma} \text{FID}(\hat{p}_{\gamma}, \hat{p}_{c \rightarrow c'}^*)}. \quad (52)$$

The Fréchet Inception Distance (FID) measures the difference between two multivariate Gaussian distributions fitted to the input empirical distributions. For two distributions p and q with means μ_p, μ_q and covariances Σ_p, Σ_q , it is given by

$$\text{FID}(p, q) = \|\mu_p - \mu_q\|_2^2 + \text{Tr} \left(\Sigma_p + \Sigma_q - 2(\Sigma_p \Sigma_q)^{1/2} \right). \quad (53)$$

rSD The Sinkhorn Divergence ratio (rSD) is defined as

$$\text{rSD} = \frac{\text{SD}_{\varepsilon}(\hat{p}_{c \rightarrow c'}^*, \hat{p}_{c \rightarrow c'})}{\min_{\gamma} \text{SD}_{\varepsilon}(\hat{p}_{\gamma}, \hat{p}_{c \rightarrow c'}^*)}. \quad (54)$$

The Sinkhorn Divergence $\text{SD}_{\varepsilon}(p, q)$ is an entropically regularized optimal transport divergence between two distributions p and q :

$$\text{SD}_{\varepsilon}(p, q) = W_{2, \varepsilon}^2(p, q) - \frac{1}{2} (W_{2, \varepsilon}^2(p, p) + W_{2, \varepsilon}^2(q, q)), \quad (55)$$

where $W_{2, \varepsilon}$ denotes the entropically regularized Wasserstein-2 distance with regularization strength ε . The regularization smooths the optimal transport problem by adding an entropy term, which makes computation more tractable. As $\varepsilon \rightarrow 0$, SD_{ε} converges to the squared Wasserstein distance W_2^2 , while for large ε , it approaches the squared Maximum Mean Discrepancy (MMD) (Feydy et al., 2019).

D.3. Challenges of evaluation on real data

The use of real scRNA-seq data is essential to assess how our model performs under realistic conditions — i.e., on data of the kind it is ultimately intended to be applied to. However, we emphasize that such datasets lack definitive ground truth labels. In our experiments, we use *cell type* and *stimulation* annotations both as concepts for intervention and as targets for evaluation in our ratio-based metrics. These labels, however, are not perfectly accurate: cell type annotations are inherently noisy and error-prone, and even for stimulation conditions, cells may have been exposed to the treatment but failed to exhibit a transcriptional response. To illustrate this, we analyze the Kang *et al.* dataset.

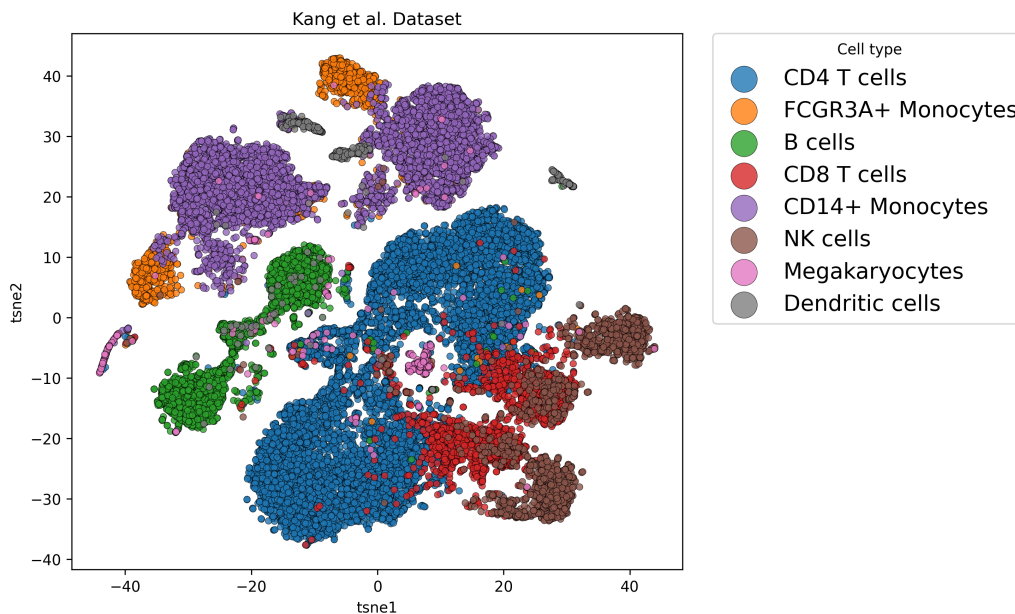


Figure 9. t-SNE of the Kang *et al.* dataset using the original cell type labels. Each point corresponds to a single cell, colored by its annotated cell type.

As shown in Figure 9, several annotated cell types exhibit strong overlap in the embedding space, most notably NK cells and CD8 T cells. To quantify this overlap, we performed a pairwise 5-fold stratified cross-validation analysis. Specifically, we trained a logistic regression model to discriminate between each pair of cell types using their PCA representations and evaluated the performance on held-out sets using the misclassification error rate. As detailed in Table 10, several pairs yield high error rates, indicating that these classes are not linearly separable—likely due to biological similarity in underlying cell states or noise in the original annotations. These results provide context for instances where ratio-based metrics exceed one, as the lack of clear separation complicates distinct cluster definition. Notably, CD8 T cells and NK cells, FCGR3A+ Monocytes and CD14+ Monocytes, and FCGR3A+ Monocytes and Dendritic cells represent the most difficult pairs to resolve.

	B cells	CD4 T cells	CD8 T cells	CD14+ Monocytes	Dendritic cells	FCGR3A+ Monocytes	Megakaryocytes	NK cells
B cells	NaN	0.40%	0.50%	0.11%	2.09%	1.09%	0.97%	0.36%
CD4 T cells	0.40%	NaN	2.43%	0.17%	0.13%	0.25%	0.80%	0.29%
CD8 T cells	0.50%	2.43%	NaN	0.10%	0.29%	0.42%	1.23%	8.90%
CD14+ Monocytes	0.11%	0.17%	0.10%	NaN	1.04%	7.07%	1.01%	0.12%
Dendritic cells	2.09%	0.13%	0.29%	1.04%	NaN	4.00%	2.94%	0.00%
FCGR3A+ Monocytes	1.09%	0.25%	0.42%	7.07%	4.00%	NaN	2.30%	0.45%
Megakaryocytes	0.97%	0.80%	1.23%	1.01%	2.94%	2.30%	NaN	0.77%
NK cells	0.36%	0.29%	8.90%	0.12%	0.00%	0.45%	0.77%	NaN

Table 10. Pairwise misclassification rates (%). Values are means from 5-fold stratified cross-validation using logistic regression on the top 50 PCs of held-out test sets.

D.4. Neural Architectures and training parameters

This section details the neural network architectures, training hyper-parameters, and general experimental settings for scCBGM and the Flow Matching (FM) models used in our experiments. When possible for each model, gene expression data was reduced to 128 principal components (PCs), which were computed exclusively from the training data to prevent data leakage.

scCBGM Model The scCBGM encoder consisted of 4 hidden layers, each with 1024 neurons. These layers incorporated residual connections, layer normalization, and dropout ($p = 0.1$). The encoder mapped gene expression (represented by 128 PCs) to a latent space of 2×128 dimensions (128 for μ and for σ). From the sampled latent variable $z \sim \mathcal{N}(\mu, \sigma)$, the concept bottleneck layers produced the known concepts (whose dimensions varied by experiment) and a default of 128 unknown concepts. The decoder mirrored the encoder’s structure with 4 layers of 1024 neurons, layer normalization, and dropout. It utilized residual connections for processing unknown concepts and direct skip connections for known concepts, as described in the main text.

scCBGM was trained for 200 epochs with a batch size of 128. Optimization was performed using Adam, starting with a learning rate of $5 \cdot 10^{-4}$ and an exponential learning rate scheduler with a decay rate of 0.997. The loss function coefficients were set as follows: concept loss at 0.1, orthogonality loss (for cross-covariance) at 0.5, and the KL divergence for μ and σ at $1 \cdot 10^{-5}$.

Flow Matching (FM) Models Both scCBGM-FM and Vanilla FM models employed a 4-layer fully-connected network, each layer comprising 1024 neurons. Similar to scCBGM, these networks included residual connections, layer normalization, and dropout. Covariates, which were either scCBGM’s known and unknown concepts (for scCBGM-FM) or the ground-truth known concepts (for Vanilla FM), were fed into the model via a learned embedding layer designed to match the hidden dimension of 1024. All FM models were trained for 200 epochs with a batch size of 128. Optimization used Adam, with an initial learning rate of $3 \cdot 10^{-4}$ and an exponential learning rate scheduler with a decay rate of 0.997. Classifier-free guidance was not utilized, as no significant performance benefit was observed.

Baseline Models We also implemented a conditional VAE (cVAE) for ablation purposes. To ensure a fair comparison, these models utilized the same backbone architecture and training hyperparameters as the CBGM model described above. All other external baseline models, including biolord, CINEMTA-OT, and scGen, were trained using their respective default parameters as specified in their original implementations.

Reconstruction Validation We further validated the ability of these architectures to faithfully reconstruct single-cell data. As shown in Figure 10, scCBGM and scCBGM-FM reliably decode the dataset, preserving both global structure and local density. In contrast, Vanilla-FM exhibits poor reconstruction fidelity, demonstrating the limitations of conditioning solely on coarse labels compared to our granular latent approach. For Vanilla-FM, reconstruction was evaluated by generating a sample from random noise conditioned on the cell’s observed concepts and comparing it to the original expression profile. As expected, since this model lacks access to cell-specific identity, it yields high MSE despite generating biologically plausible samples. This baseline highlights the necessity of the scCBGM latent representation for preserving individual cell identity during the encoding-decoding process.

D.5. Benchmark on synthetic data

For the synthetic data benchmark, we used the same architectural design and hyperparameters as described in Appendix D.4. We ran the experiments on the three datasets outlined in Appendix C.5, each with 5 interventions and 4 random seeds.

D.6. Performance and number of concepts

While only the concepts on which one intends to *intervene* need to be explicitly characterized in the *known concept layer*, the total number of concepts can increase rapidly when modeling complex biological systems. To further assess how scCBGM scales with the number of concepts, we generated three additional synthetic datasets using the same hyperparameters as *Synthetic 1* (see Appendix C.5), varying only the number of concepts. This setup enables a controlled evaluation of how concept dimensionality influences model performance.

As shown in Table 12, performance decreases only marginally—by less than 2%—as the number of concepts increases.

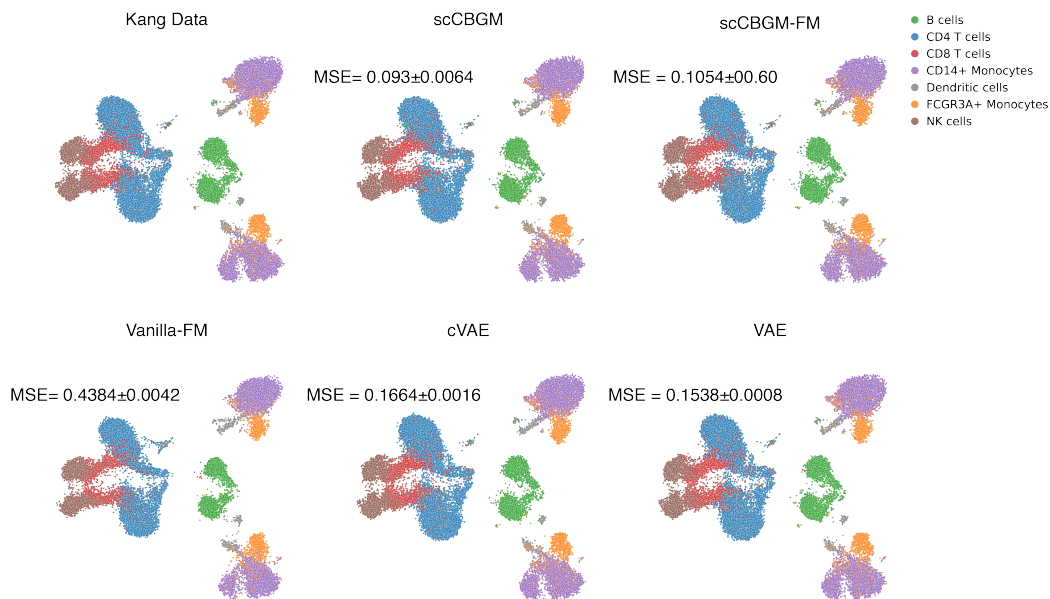


Figure 10. **Qualitative and quantitative comparison of data reconstruction.** UMAP visualizations of the Kang dataset (top-left) and reconstructions from five generative models. Points are colored by cell type. scCBGM and scCBGM-FM successfully reproduce the data distribution with low test-set MSE. Vanilla-FM shows poor reconstruction fidelity due to a lack of granular conditioning, while cVAE and VAE achieve moderate accuracy. MSE values are means and standard deviations over 5 random initialization seeds for each model.

	Synthetic 1	Synthetic 2	Synthetic 3
scCBGM	0.0388±0.0053	0.0318±0.0071	0.0407±0.0027
scCBGM-FM (edit)	0.0025±0.0016	0.0028±0.0014	0.0039±0.0023
scCBGM-FM (decode)	0.0539±0.0039	0.0444±0.0082	0.0594±0.0092
Vanilla-FM (edit)	0.0031±0.0014	0.0049±0.0016	0.0049±0.0027
Vanilla-FM (decode)	0.0756±0.0014	0.0769±0.0014	0.0773±0.0041
CINEMA-OT	0.0390±0.0025	0.0393±0.0012	0.0400±0.0034
biolord	0.0402±0.0014	0.0411±0.0021	0.0428±0.0021

Table 11. Comparison of methods on synthetic data. We evaluate in PCA space to account for different normalization strategies, so scCBGM values differ from Table 15. Values are MSE (mean ± std), averaged over interventions (5) and seeds (4).

This trend is consistent with prior observations in the literature (Ismail et al., 2025), indicating that the model remains stable and effective even as the concept space expands.

concepts	MSE
5	0.19617 ± 0.00195
20	0.19597 ± 0.00089
100	0.19846 ± 0.00081
250	0.19809 ± 0.00053

Table 12. Performance under varying numbers of concepts. Values are reported as mean \pm standard deviation, computed across three random seeds and five interventions. No noise was introduced in the concept annotations.

D.7. Concept leakage

The **cross-covariance loss** between the known and unknown concepts is introduced to prevent information leakage between the two layers. This effect is supported by our results in Section 5 and the theoretical justification in Appendix B.1. To examine this question more directly, we designed an experiment that mimics a realistic scenario in which relevant concepts are *not* included among the known ones and must instead be captured by the unknown layer, followed by an examination of how intervening on the known concepts impacted the state of the unknown ones.

In this experiment, we used the **Kang et al.** dataset (Appendix D.1.1). Only the *binary stimulation concept* was included in the model — i.e., cell-type information was *not* encoded in the known layer. The data was split into a 60/40 train/test partition. We trained SCCBGM with the single stimulation concept, along with two separate classifiers: (i) a one-vs-all classifier predicting **cell type** from the learned expression representation, and (ii) a binary classifier predicting whether a cell was **stimulated** or **control**.

For evaluation, we took the test data and, within each cell type, *intervened* on all unstimulated (control) cells by setting their stimulation state to “on.” We then applied the two classifiers—trained on the original training data—to predict cell type and stimulation status for each cell *before* and *after* the intervention.

If concept leakage has been effectively prevented, the **stimulation predictions** should switch from 0 to 1, while the **cell-type predictions** should remain stable. This behavior is clearly observed in Figure 11, where the stimulation scores shift from low to high after intervention, whereas the cell-type scores remain largely unchanged. The corresponding quantitative results are summarized in Table 13.

	f(cell type)		f(stim)	
	Bef.	Aft.	Bef.	Aft.
B cells	0.983	0.977	0.004	1.000
CD14+ Mono.	0.971	0.938	0.002	1.000
CD4 T cells	0.985	0.988	0.009	1.000
CD8 T cells	0.718	0.691	0.014	1.000
FCGR3A+ Mon.	0.750	0.777	0.000	1.000
NK cells	0.902	0.945	0.022	1.000

Table 13. Mean classifier scores before/after intervention (test data).

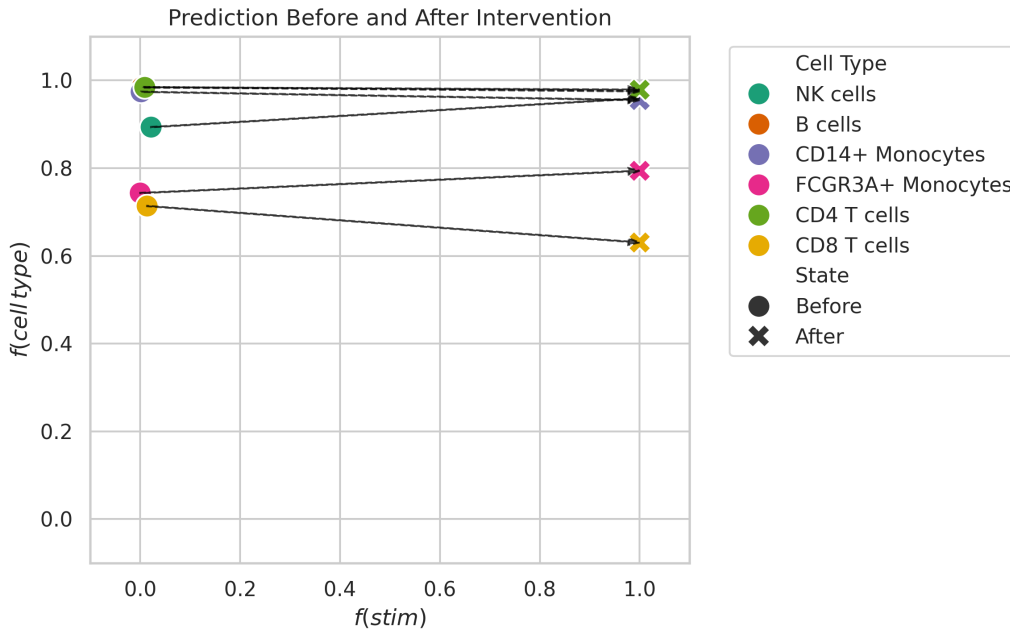


Figure 11. Results from classifiers trained to predict cell type and stimuli applied to the test data before and after intervention. Values are reported as mean across all cells in the test data. Each color represents a cell type. Good results are straight lines from left to right.

Furthermore, we performed an isolation experiment on the Kang et al. dataset using the stimulation label. Specifically, we compared two scCBGM models: one where stimulation was included as a known concept, and another where it was excluded. A logistic regression classifier (via 5-fold cross-validation) was trained to predict the stimulation state from the unknown embeddings. When stimulation is explicitly modeled, the classifier’s performance drops from an AUROC of 0.9988 to 0.5580, 14. This stark reduction confirms that the known categorical variation is effectively isolated and decoupled

from the residual unknown layer.

	Fold 1	Fold 2	Fold 3	Fold 4	Fold 5	Mean \pm Std
Stim in Known	0.572	0.577	0.555	0.545	0.541	0.5580 \pm 0.0160
Stim in Unknown	0.998	1.000	0.998	0.999	0.999	0.9988 \pm 0.0008

Table 14. Classifier performance (AUROC) across a 5-fold cross-validation isolation experiment.

D.8. Ablations

D.8.1. ARCHITECTURE ABLATIONS SYNTHETIC DATA

Model	Bottleneck	Skip	\mathcal{L}	MSE
CBGM	CBM	✓	\mathcal{L}_{\cosine}	0.1989 \pm 0.00023
	CEM	✓	\mathcal{L}_{cc}	0.19865 \pm 0.00023
	CEM	✓	\mathcal{L}_{\cosine}	0.19816 \pm 0.00022
	CEM	✗	\mathcal{L}_{cc}	0.1981 \pm 0.0002
	CEM	✗	\mathcal{L}_{\cosine}	0.19804 \pm 0.00021
	CEM	✗	\mathcal{L}_{cc}	0.19791 \pm 0.00021
scCBGM	CBM	✓	\mathcal{L}_{cc}	0.19655\pm0.00019

Table 15. Ablation study over the skip connections and cross-covariance loss. MSE between true and predicted counterfactuals, averaged over datasets (3), interventions (3), noise levels (2), types of noise (5), and seeds (2). We report values as Mean \pm SEM.

We compare the contribution of each individual component across a $2 \times 2 \times 2$ design space of Bottleneck (CEM vs. CBM), Skip Connection (yes or no), Loss (cross-covariance vs. cosine). On the synthetic data we are able to do cell-level evaluation, something that real data does not permit. We evaluate each model across: 3 different datasets, 5 different types of interventions (in each dataset), 2 random seeds, 5 different types of noise, and 2 different levels of noise. For comparable results, we used the exact same hyperparameters across all configurations except for the ablated components. However, we highlight that the models using a cosine loss are restricted to using the same number of known as unknown concepts, a limit not imposed on the cross-covariance loss.

D.8.2. ARCHITECTURE ABLATIONS ON REAL DATA

In Table 16, we report the result of our model architecture ablations on the Kang et al. (2017) dataset. This experiment confirms the need for the disentanglement loss and the skip connection in scCBGM.

Table 16. rMMD over all subtypes on the Kang et al. (2017) dataset, for different ablations of scCBGM ordered mean in descending order. We evaluate different choices of bottleneck architecture, the presence of skip connection and different disentanglement losses (cosine similarity, cross-covariance, or no disentanglement loss (left blank)). We report values as Mean \pm SEM, and report the average rMMD over all subtypes for each method (Mean column). Best model for each subtype is bolded. The scCBGM configurations used in our benchmarks are highlighted in the Method column.

Method	Bottleneck	Skip	\mathcal{L}	B Cells		Cd14		Cd4			Cd8		Dendritic		Fcgr3A		Nk	Mean
				subtype 0	subtype 1	subtype 0	subtype 1	subtype 0	subtype 1	subtype 2	subtype 0	subtype 1	subtype 0	subtype 1	subtype 0	subtype 1		
CEM	✓	✓	\mathcal{L}_{cc}	2.859 \pm 0.560	1.484 \pm 0.348	11.505 \pm 1.676	9.367 \pm 0.917	4.294 \pm 0.864	6.938 \pm 2.221	2.264 \pm 0.511	2.575 \pm 0.174	5.936 \pm 1.966	2.159 \pm 0.244	1.779 \pm 0.164	1.663 \pm 0.073	24.590 \pm 1.246	1.911 \pm 0.094	5.666
CEM	✓	✓	\mathcal{L}_{\cosine}	1.456 \pm 0.266	1.154 \pm 0.143	8.753 \pm 0.244	8.449 \pm 0.728	3.103 \pm 0.031	4.401 \pm 0.609	1.178 \pm 0.125	2.604 \pm 0.169	2.676 \pm 0.350	1.133 \pm 0.163	1.603 \pm 0.164	1.777 \pm 0.087	20.765 \pm 1.889	1.917 \pm 0.517	4.355
CEM	✓	✓		1.257 \pm 0.063	0.930 \pm 0.126	9.026 \pm 0.429	7.466 \pm 0.548	2.674 \pm 0.441	3.970 \pm 0.246	1.133 \pm 0.032	2.271 \pm 0.085	2.434 \pm 0.275	1.394 \pm 0.120	1.762 \pm 0.244	1.159 \pm 0.061	22.574 \pm 3.052	1.391 \pm 0.187	4.246
CBM	✗	✓	\mathcal{L}_{cc}	1.078 \pm 0.011	0.758 \pm 0.007	9.634 \pm 0.078	7.544 \pm 0.100	2.081 \pm 0.010	3.321 \pm 0.040	0.809 \pm 0.022	1.788 \pm 0.007	1.674 \pm 0.012	1.436 \pm 0.010	1.449 \pm 0.012	1.684 \pm 0.015	22.232 \pm 0.202	1.067 \pm 0.008	4.038
CBM	✗	✓	\mathcal{L}_{\cosine}	1.111 \pm 0.123	1.134 \pm 0.247	4.007 \pm 2.175	1.647 \pm 0.134	1.664 \pm 0.264	10.931 \pm 3.377	1.276 \pm 0.028	3.942 \pm 1.281	2.650 \pm 0.258	1.324 \pm 0.221	1.527 \pm 0.246	1.380 \pm 0.296	14.633 \pm 7.135	5.634 \pm 0.890	3.776
CBM	✗	✗	\mathcal{L}_{cc}	0.977 \pm 0.012	0.639 \pm 0.008	9.001 \pm 0.045	6.776 \pm 0.056	1.719 \pm 0.072	2.797 \pm 0.066	0.703 \pm 0.003	1.578 \pm 0.023	1.372 \pm 0.022	1.336 \pm 0.015	1.310 \pm 0.022	1.467 \pm 0.021	20.841 \pm 0.071	0.953 \pm 0.018	3.676
CBM	✗	✗	\mathcal{L}_{\cosine}	1.060 \pm 0.062	0.877 \pm 0.048	7.820 \pm 0.228	6.365 \pm 0.218	2.036 \pm 0.135	3.496 \pm 0.164	1.058 \pm 0.072	2.032 \pm 0.136	1.896 \pm 0.083	1.336 \pm 0.028	1.741 \pm 0.093	1.387 \pm 0.119	17.643 \pm 0.650	1.310 \pm 0.065	3.575
CBM	✗	✗	\mathcal{L}_{cc}	1.137 \pm 0.132	0.823 \pm 0.066	6.488 \pm 0.284	5.767 \pm 0.103	1.703 \pm 0.071	3.088 \pm 0.214	0.937 \pm 0.093	1.999 \pm 0.061	1.723 \pm 0.051	1.196 \pm 0.032	1.560 \pm 0.153	1.400 \pm 0.043	16.781 \pm 0.306	1.793 \pm 0.092	3.314
CBGM	✓	✓	\mathcal{L}_{cc}	1.057 \pm 0.052	0.866 \pm 0.056	7.270 \pm 0.435	5.371 \pm 0.412	1.761 \pm 0.084	3.268 \pm 0.295	1.152 \pm 0.029	1.829 \pm 0.062	2.024 \pm 0.185	1.225 \pm 0.085	1.621 \pm 0.074	1.305 \pm 0.034	14.960 \pm 0.971	1.165 \pm 0.222	3.205
CBM	✗	✗	\mathcal{L}_{\cosine}	1.156 \pm 0.339	1.148 \pm 0.630	5.739 \pm 2.045	1.599 \pm 0.340	2.371 \pm 1.264	1.647 \pm 0.485	0.609 \pm 0.030	0.928 \pm 0.121	1.260 \pm 0.196	1.118 \pm 0.298	1.943 \pm 0.534	1.437 \pm 0.189	9.970 \pm 2.096	0.791 \pm 0.114	2.265
scCBGM	✓	✓	\mathcal{L}_{cc}	0.153 \pm 0.004	0.103 \pm 0.005	1.195 \pm 0.058	1.069 \pm 0.061	0.155 \pm 0.008	0.279 \pm 0.015	0.076 \pm 0.004	0.182 \pm 0.010	0.165 \pm 0.014	0.390 \pm 0.011	0.359 \pm 0.039	0.166 \pm 0.007	3.151 \pm 0.318	0.921 \pm 0.244	0.598
CBM	✗	✗	\mathcal{L}_{cc}	0.175 \pm 0.004	0.103 \pm 0.007	0.751 \pm 0.082	1.142 \pm 0.030	0.201 \pm 0.012	0.297 \pm 0.023	0.096 \pm 0.011	0.221 \pm 0.010	0.198 \pm 0.011	0.430 \pm 0.018	0.343 \pm 0.059	0.202 \pm 0.012	3.474 \pm 0.129	0.166 \pm 0.009	0.557

D.8.3. VARIATIONAL AUTO-ENCODER VS. AUTO-ENCODER

In figure 12, we present a performance comparison between scCBGM and an ablated version of scCBGM where the variational auto-encoder backbone has been replaced with a simple auto-encoder (scCBGM(ae)). We found that the rMMD values on

different cell populations of the Kang et al. (2017) dataset were typically lower (better) with a variational auto-encoder backbone than without.

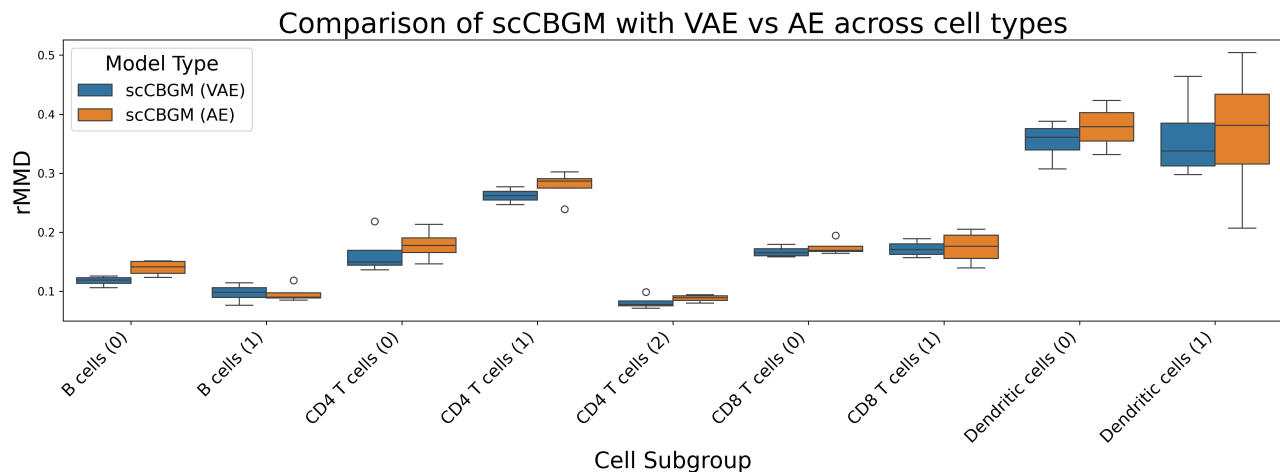


Figure 12. Comparison of rMMD performance between two versions of the auto-encoder backbone of scCBGM: a variational auto-encoder (VAE) and a regular auto-encoder (AE). The boxplots are computed over 4 seeds for each cell population from the Kang et al. (2017) dataset. Lower rMMD is better.

D.9. Additional benchmarking results

D.9.1. COUNTER-FACTUAL MODELING PREDICTS CELLULAR RESPONSE TO PERTURBATION

Tables 17 and 18 show results on the Kang et al. (2017) dataset on the rFID and rSD metrics. Similarly to our rMMD results in the main text, we find that our model outperforms other baselines in 5 out of 7 experiments.

Table 17. rFID (Mean \pm SEM) per cell group for different models (best, second-best, and third-best bolded) in the Kang et al. (2017) dataset.

Model	B cells	T cells (CD4)	T cells (CD8)	Monocytes (FCGR3A)	Monocytes (CD14)	Dendritic Cells	NK cells
scCBGM	0.265 \pm 0.003	0.277 \pm 0.003	0.515 \pm 0.004	1.135 \pm 0.044	1.719 \pm 0.032	0.702 \pm 0.010	1.230 \pm 0.285
scCBGM-FM (decode)	0.247 \pm 0.002	0.253 \pm 0.001	0.457 \pm 0.003	0.996 \pm 0.040	1.769 \pm 0.051	0.665 \pm 0.009	0.215 \pm 0.006
scCBGM-FM (edit)	0.248 \pm 0.002	0.241 \pm 0.003	0.472 \pm 0.009	0.971 \pm 0.018	1.723 \pm 0.038	0.670 \pm 0.005	0.202 \pm 0.001
CBGM	1.086 \pm 0.053	2.031 \pm 0.059	2.142 \pm 0.041	5.244 \pm 0.112	5.353 \pm 0.123	1.634 \pm 0.031	1.664 \pm 0.174
Vanilla-FM (decode)	0.937 \pm 0.013	0.953 \pm 0.002	0.999 \pm 0.013	1.995 \pm 0.009	1.589 \pm 0.043	2.017 \pm 0.026	0.215 \pm 0.001
Vanilla-FM (edit)	0.551 \pm 0.012	0.452 \pm 0.007	0.584 \pm 0.007	1.233 \pm 0.039	1.341 \pm 0.011	1.300 \pm 0.033	0.177 \pm 0.003
biolord	1.730 \pm 0.001	3.219 \pm 0.001	3.039 \pm 0.006	3.978 \pm 0.009	1.855 \pm 0.003	1.979 \pm 0.002	1.949 \pm 0.001
biolord-FM	1.165 \pm 0.003	1.782 \pm 0.002	1.613 \pm 0.004	5.446 \pm 0.011	7.439 \pm 0.020	1.986 \pm 0.004	1.049 \pm 0.004
Cinema-OT	1.500 \pm 0.001	3.563 \pm 0.001	3.077 \pm 0.003	3.550 \pm 0.004	4.637 \pm 0.002	0.928 \pm 0.000	2.565 \pm 0.003
scGen	1.275 \pm 0.003	2.732 \pm 0.010	2.833 \pm 0.013	2.567 \pm 0.014	2.801 \pm 0.081	0.883 \pm 0.010	1.966 \pm 0.022
CVAE	0.653 \pm 0.006	1.002 \pm 0.007	1.068 \pm 0.019	4.075 \pm 0.016	4.553 \pm 0.034	1.216 \pm 0.013	0.732 \pm 0.007
CVAE-FM (decode)	0.568 \pm 0.005	0.812 \pm 0.006	0.948 \pm 0.006	3.608 \pm 0.023	4.257 \pm 0.029	1.109 \pm 0.010	0.623 \pm 0.006
CVAE-FM (edit)	0.563 \pm 0.002	0.803 \pm 0.004	0.933 \pm 0.003	3.723 \pm 0.014	4.213 \pm 0.035	1.123 \pm 0.007	0.600 \pm 0.003

D.9.2. COMPOSITIONAL GENERALIZATION WITH MANY STIMULI

Tables 19 and 20 show results on rFID and rSD on the Cui et al. (2024) dataset. Similarly to our rMMD results in the main text, we find that our model outperforms other baselines in 4 out of 7 experiments.

The Cui et al. (2024) dataset contains 17 cell types with 86 cytokines perturbations, leading to 1479 possible configurations. To keep experiments concise, we focused on seven pairs that the original study identified as inducing significant transcriptional shifts, ensuring a robust signal for evaluation.

scCBGM: Interpretable Single-Cell Counterfactual Editing

Table 18. rSD (Mean \pm SEM) per cell group for different models (**best**, **second-best**, and **third-best** bolded) in the Kang et al. (2017) dataset.

Model	B cells	T cells (CD4)	T cells (CD8)	Monocytes (FCGR3A)	Monocytes (CD14)	Dendritic Cells	NK cells
scCBGM	0.393 \pm 0.004	0.507 \pm 0.004	0.971 \pm 0.006	0.968 \pm 0.028	1.246 \pm 0.033	0.744 \pm 0.010	1.135 \pm 0.254
scCBGM-FM (decode)	0.387 \pm 0.014	0.515 \pm 0.005	0.853 \pm 0.015	0.868 \pm 0.023	1.312 \pm 0.046	0.742 \pm 0.013	0.290 \pm 0.023
scCBGM-FM (edit)	0.387 \pm 0.002	0.500 \pm 0.002	0.960 \pm 0.013	0.838 \pm 0.012	1.261 \pm 0.040	0.726 \pm 0.003	0.293 \pm 0.003
CBGM	1.046 \pm 0.057	1.824 \pm 0.048	1.865 \pm 0.010	3.432 \pm 0.024	4.401 \pm 0.124	1.677 \pm 0.008	1.446 \pm 0.130
Vanilla-FM (decode)	1.089 \pm 0.029	1.042 \pm 0.003	1.336 \pm 0.044	1.484 \pm 0.020	1.165 \pm 0.038	2.062 \pm 0.038	0.436 \pm 0.031
Vanilla-FM (edit)	0.662 \pm 0.011	0.750 \pm 0.011	1.124 \pm 0.018	1.025 \pm 0.019	0.916 \pm 0.010	1.431 \pm 0.032	0.318 \pm 0.012
biolord	0.888 \pm 0.002	0.897 \pm 0.002	0.878 \pm 0.001	1.405 \pm 0.004	0.371 \pm 0.001	1.570 \pm 0.001	0.444 \pm 0.002
biolord-FM	1.283 \pm 0.016	1.694 \pm 0.005	1.785 \pm 0.021	3.765 \pm 0.012	6.414 \pm 0.030	1.937 \pm 0.009	1.114 \pm 0.022
Cinema-OT	0.840 \pm 0.001	1.593 \pm 0.004	1.154 \pm 0.003	1.591 \pm 0.002	3.241 \pm 0.007	0.700 \pm 0.001	1.195 \pm 0.007
scGen	0.967 \pm 0.005	1.876 \pm 0.012	1.872 \pm 0.007	1.454 \pm 0.019	1.979 \pm 0.075	0.796 \pm 0.010	1.366 \pm 0.014
CVAE	0.730 \pm 0.005	1.192 \pm 0.018	1.422 \pm 0.030	2.914 \pm 0.030	3.846 \pm 0.029	1.265 \pm 0.010	0.767 \pm 0.009
CVAE-FM (decode)	0.670 \pm 0.005	0.959 \pm 0.011	1.213 \pm 0.036	2.527 \pm 0.032	3.601 \pm 0.022	1.206 \pm 0.019	0.666 \pm 0.018
CVAE-FM (edit)	0.643 \pm 0.004	1.010 \pm 0.008	1.309 \pm 0.012	2.665 \pm 0.015	3.544 \pm 0.036	1.181 \pm 0.009	0.646 \pm 0.002

Table 19. rFID (Mean \pm SEM) per cell group for different models (**best**, **second-best**, and **third-best** bolded) in the Cui et al. (2024) dataset.

Model	T cells (Gamma-delta)	T cells (CD4)	T cells (CD8)	Dendritic (cDC2)	Dendritic (Langerhans)	Myeloid (Macrophages)	Lymphoid (NK cells)
scCBGM	0.688 \pm 0.006	0.523 \pm 0.003	0.474 \pm 0.007	0.851 \pm 0.007	0.162 \pm 0.002	1.263 \pm 0.019	1.941 \pm 0.021
scCBGM-FM (decode)	0.731 \pm 0.007	0.555 \pm 0.003	0.509 \pm 0.005	0.875 \pm 0.008	0.170 \pm 0.002	1.276 \pm 0.004	1.956 \pm 0.008
scCBGM-FM (edit)	0.751 \pm 0.005	0.570 \pm 0.003	0.508 \pm 0.003	0.869 \pm 0.008	0.169 \pm 0.001	1.319 \pm 0.008	1.985 \pm 0.015
CBGM	0.884 \pm 0.091	0.588 \pm 0.025	0.488 \pm 0.015	0.840 \pm 0.056	0.167 \pm 0.004	1.555 \pm 0.160	2.335 \pm 0.070
Vanilla-FM (decode)	1.527 \pm 0.040	1.474 \pm 0.090	1.470 \pm 0.057	1.223 \pm 0.055	1.472 \pm 0.044	4.001 \pm 0.253	2.124 \pm 0.110
Vanilla-FM (edit)	0.875 \pm 0.020	0.644 \pm 0.009	0.510 \pm 0.016	0.646 \pm 0.049	0.478 \pm 0.045	3.518 \pm 0.169	1.014 \pm 0.044
biolord	2.164 \pm 0.003	1.412 \pm 0.001	1.265 \pm 0.001	1.223 \pm 0.000	0.999 \pm 0.000	4.400 \pm 0.013	2.612 \pm 0.006
biolord-FM	1.357 \pm 0.007	1.117 \pm 0.005	1.056 \pm 0.009	1.577 \pm 0.003	1.125 \pm 0.010	1.859 \pm 0.009	2.634 \pm 0.019
Cinema-OT	1.655 \pm 0.002	1.056 \pm 0.001	1.127 \pm 0.001	0.976 \pm 0.001	0.816 \pm 0.000	4.187 \pm 0.015	5.729 \pm 0.007
scGen	1.601 \pm 0.011	1.405 \pm 0.009	1.070 \pm 0.013	0.830 \pm 0.004	0.291 \pm 0.002	2.053 \pm 0.005	2.767 \pm 0.008
CVAE	0.730 \pm 0.004	0.525 \pm 0.002	0.470 \pm 0.002	0.930 \pm 0.003	0.167 \pm 0.001	1.312 \pm 0.006	2.047 \pm 0.016
CVAE-FM (decode)	0.754 \pm 0.005	0.559 \pm 0.002	0.511 \pm 0.004	0.929 \pm 0.003	0.176 \pm 0.001	1.288 \pm 0.008	2.048 \pm 0.006
CVAE-FM (edit)	0.778 \pm 0.002	0.571 \pm 0.004	0.507 \pm 0.005	0.938 \pm 0.001	0.177 \pm 0.000	1.351 \pm 0.002	2.093 \pm 0.005

For completeness, we still ran an extensive comparison analysis between scCBGM-FM (edit) and CVAE-FM (edit) over all 1479 cell-types - interventions pairs in the dataset with a single seed. Running all baselines was prohibitive (both models require 850 GPU hours each). We thus chose the two most competitive models on the seven pairs from the main analyses. Aggregated results per cell-type (over cytokine perturbations) are presented in Figure 13. Using a paired t-test over all 1479 configurations, scCBGM-FM was found to significantly outperform CVAE-FM across the full intervention space ($p\text{-val} < 1e^{-10}$) for all metrics.

D.9.3. COMPLETE NAULT ET AL. (2023) RESULTS

In Tables 21, 22, and 23 we report the results of our experiment on the Nault et al. (2023) dataset on all available cell types for the rMMD, rFID, and rSD metrics respectively.

scCBGM: Interpretable Single-Cell Counterfactual Editing

Table 20. rSD (Mean \pm SEM) per cell group for different models (best, second-best, and third-best bolded) in the Cui et al. (2024) dataset.

Model	T cells (Gamma-delta)	T cells (CD4)	T cells (CD8)	Dendritic (cDC2)	Dendritic (Langerhans)	Myeloid (Macrophages)	Lymphoid (NK cells)
scCBGM	0.781 \pm 0.018	0.684 \pm 0.004	0.704 \pm 0.011	0.852 \pm 0.012	0.194 \pm 0.005	1.301 \pm 0.024	1.898 \pm 0.015
scCBGM-FM (decode)	0.822 \pm 0.010	0.757 \pm 0.011	0.808 \pm 0.013	0.866 \pm 0.010	0.204 \pm 0.002	1.326 \pm 0.015	1.915 \pm 0.014
scCBGM-FM (edit)	0.858 \pm 0.003	0.756 \pm 0.001	0.747 \pm 0.003	0.872 \pm 0.007	0.208 \pm 0.002	1.343 \pm 0.008	1.984 \pm 0.013
CBGM	0.936 \pm 0.122	0.767 \pm 0.033	0.680 \pm 0.029	0.836 \pm 0.056	0.196 \pm 0.002	1.520 \pm 0.101	2.272 \pm 0.049
Vanilla-FM (decode)	1.503 \pm 0.024	1.678 \pm 0.038	2.127 \pm 0.069	1.212 \pm 0.049	1.454 \pm 0.035	3.455 \pm 0.155	2.040 \pm 0.121
Vanilla-FM (edit)	1.005 \pm 0.011	0.873 \pm 0.020	0.819 \pm 0.029	0.636 \pm 0.045	0.511 \pm 0.050	3.105 \pm 0.108	0.964 \pm 0.038
biolord	1.099 \pm 0.001	0.778 \pm 0.001	0.785 \pm 0.002	0.897 \pm 0.001	0.795 \pm 0.000	2.287 \pm 0.007	1.537 \pm 0.005
biolord-FM	1.431 \pm 0.019	1.359 \pm 0.022	1.526 \pm 0.033	1.530 \pm 0.004	1.132 \pm 0.010	2.019 \pm 0.016	2.525 \pm 0.030
Cinema-OT	1.240 \pm 0.003	0.869 \pm 0.002	1.105 \pm 0.002	0.918 \pm 0.001	0.792 \pm 0.001	3.138 \pm 0.010	4.971 \pm 0.028
scGen	0.999 \pm 0.010	1.044 \pm 0.009	0.821 \pm 0.017	0.689 \pm 0.002	0.205 \pm 0.002	1.496 \pm 0.007	2.119 \pm 0.009
CVAE	0.852 \pm 0.005	0.717 \pm 0.001	0.688 \pm 0.005	0.928 \pm 0.003	0.204 \pm 0.003	1.356 \pm 0.012	2.035 \pm 0.015
CVAE-FM (decode)	0.878 \pm 0.016	0.733 \pm 0.008	0.750 \pm 0.017	0.919 \pm 0.004	0.214 \pm 0.006	1.383 \pm 0.019	2.016 \pm 0.028
CVAE-FM (edit)	0.895 \pm 0.004	0.752 \pm 0.003	0.754 \pm 0.009	0.937 \pm 0.000	0.216 \pm 0.001	1.385 \pm 0.003	2.076 \pm 0.011

Table 21. rMMD (Mean \pm SEM) per model and target group (best, second-best, and third-best bolded) in Nault et al. (2023) dataset

Model	B cells	T cells	Hepatocytes Centrilobular	Endothelial cells	Stellate cell	Macrophages	Hepatocytes (Periportal)
scCBGM	0.9309 \pm 0.3402	0.8832 \pm 0.3996	0.6236 \pm 0.0114	1.1352 \pm 0.3946	0.8952 \pm 0.5483	0.6171 \pm 0.4101	0.7521 \pm 0.0457
scCBGM-FM (decode)	0.9497 \pm 0.2785	0.8368 \pm 0.3466	0.6084 \pm 0.0286	1.0465 \pm 0.3216	0.8609 \pm 0.4399	0.5960 \pm 0.3432	0.7186 \pm 0.0564
scCBGM-FM (edit)	0.9499 \pm 0.3040	0.8507 \pm 0.3719	0.6172 \pm 0.0012	1.0589 \pm 0.3438	0.8437 \pm 0.4515	0.6286 \pm 0.4083	0.7079 \pm 0.0565
Vanilla-FM (decode)	3.2153 \pm 1.6126	3.7338 \pm 2.0041	1.4582 \pm 0.6899	8.1729 \pm 2.6690	10.4811 \pm 7.0579	2.3361 \pm 1.3756	1.1853 \pm 0.4838
Vanilla-FM (edit)	1.2832 \pm 0.4411	1.4381 \pm 0.2921	0.4424 \pm 0.0877	6.8274 \pm 0.9141	7.2351 \pm 3.2392	1.2286 \pm 0.4893	1.0301 \pm 0.3172
Biolord	22.2091 \pm 9.1562	27.6154 \pm 12.7611	/	41.3361 \pm 17.3826	44.3398 \pm 32.5313	21.1511 \pm 10.7040	4.7065 \pm 2.0315
Cinema-OT	23.1503 \pm 11.3323	29.3735 \pm 15.0724	4.6668 \pm 1.5976	40.3636 \pm 20.2509	45.5700 \pm 33.2892	11.7172 \pm 4.8449	5.2949 \pm 1.3632
scGen	11.5939 \pm 5.2396	13.4637 \pm 6.5632	2.2144 \pm 0.6419	16.7187 \pm 7.2767	12.0668 \pm 9.0206	6.1012 \pm 3.3398	2.3892 \pm 0.7981
CVAE	1.263 \pm 0.072	1.328 \pm 0.060	1.842 \pm 0.809	1.625 \pm 0.121	1.349 \pm 0.281	1.104 \pm 0.229	1.554 \pm 0.433
CVAE-FM (decode)	1.005 \pm 0.102	0.870 \pm 0.091	1.333 \pm 0.585	1.018 \pm 0.110	0.882 \pm 0.117	0.852 \pm 0.015	1.143 \pm 0.263
CVAE-FM (edit)	0.938 \pm 0.101	0.887 \pm 0.161	1.337 \pm 0.569	0.963 \pm 0.102	0.853 \pm 0.171	0.909 \pm 0.122	1.131 \pm 0.253

Table 22. rFID (Mean \pm SEM) per cell group for different models (best, second-best, and third-best bolded) in the Nault et al. (2023) dataset.

Model	B cells	T cells	Hepatocytes (Centrilobular)	Endothelial cells	Stellate cell	Macrophages	Hepatocytes (Periportal)
scCBGM	1.028 \pm 0.158	0.964 \pm 0.241	0.755 \pm 0.034	1.121 \pm 0.255	1.042 \pm 0.353	0.993 \pm 0.756	0.842 \pm 0.050
scCBGM-FM (decode)	1.015 \pm 0.140	0.918 \pm 0.210	0.717 \pm 0.007	1.132 \pm 0.230	0.964 \pm 0.324	0.911 \pm 0.674	0.807 \pm 0.026
scCBGM-FM (edit)	1.022 \pm 0.151	0.942 \pm 0.224	0.727 \pm 0.006	1.156 \pm 0.250	0.964 \pm 0.332	0.957 \pm 0.723	0.810 \pm 0.036
Vanilla-FM (decode)	3.425 \pm 0.001	3.022 \pm 0.147	1.552 \pm 0.793	21.293 \pm 6.744	21.950 \pm 7.596	3.885 \pm 1.869	1.232 \pm 0.482
Vanilla-FM (edit)	1.499 \pm 0.185	1.333 \pm 0.198	0.436 \pm 0.151	17.998 \pm 3.897	14.030 \pm 2.147	1.766 \pm 0.489	1.028 \pm 0.283
biolord	5.103 \pm 0.560	5.510 \pm 0.702	/	26.211 \pm 9.435	23.090 \pm 9.283	7.530 \pm 4.283	4.353 \pm 1.775
Cinema-OT	5.414 \pm 0.918	5.841 \pm 0.928	4.035 \pm 1.900	18.180 \pm 8.224	24.920 \pm 9.252	4.808 \pm 2.321	4.335 \pm 1.276
scGen	6.018 \pm 0.665	6.498 \pm 1.000	3.246 \pm 1.460	9.912 \pm 3.031	6.016 \pm 2.582	6.495 \pm 5.042	3.457 \pm 1.269
CVAE	1.064 \pm 0.020	1.069 \pm 0.020	1.778 \pm 0.314	1.276 \pm 0.134	1.126 \pm 0.126	1.215 \pm 0.303	1.623 \pm 0.308
CVAE-FM (decode)	0.985 \pm 0.087	0.909 \pm 0.108	1.235 \pm 0.417	1.014 \pm 0.123	0.924 \pm 0.106	1.032 \pm 0.294	1.190 \pm 0.324
CVAE-FM (edit)	0.961 \pm 0.070	0.926 \pm 0.113	1.250 \pm 0.421	0.974 \pm 0.082	0.898 \pm 0.136	1.056 \pm 0.326	1.192 \pm 0.321

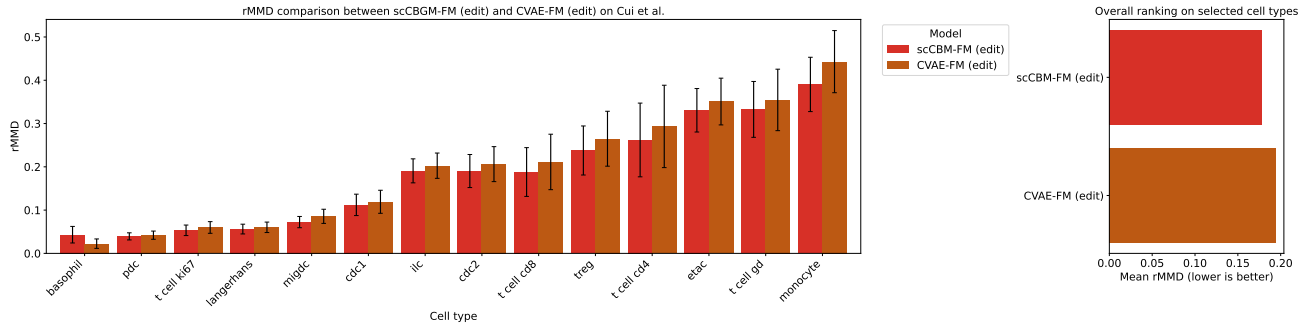


Figure 13. Comparison of scCBGM-FM (edit) and CVAE-FM (edit) on the full Cui et al. (2024) dataset. (Left) rMMD for both methods averaged per cell type over the different cytokine perturbations. (Right) Average rMMD on all cell-type-cytokine pairs.

Table 23. rSD (Mean \pm SEM) per cell group for different models (best, second-best, and third-best bolded) in the Nault et al. (2023) dataset.

Model	B cells	T cells	Hepatocytes (Centrilobular)	Endothelial cells	Stellate cell	Macrophages	Hepatocytes (Periportal)
scCBGM	0.986 \pm 0.103	0.974 \pm 0.182	0.705 \pm 0.090	1.073 \pm 0.232	1.014 \pm 0.358	0.961 \pm 0.794	0.742 \pm 0.001
scCBGM-FM (decode)	0.999 \pm 0.089	0.902 \pm 0.165	0.683 \pm 0.061	1.108 \pm 0.209	0.943 \pm 0.326	0.927 \pm 0.722	0.713 \pm 0.027
scCBGM-FM (edit)	1.021 \pm 0.084	0.968 \pm 0.170	0.704 \pm 0.089	1.154 \pm 0.230	0.914 \pm 0.342	0.959 \pm 0.763	0.712 \pm 0.016
Vanilla-FM (decode)	3.051 \pm 0.276	2.686 \pm 0.012	1.394 \pm 0.572	20.301 \pm 5.140	25.426 \pm 10.854	3.173 \pm 1.247	1.330 \pm 0.635
Vanilla-FM (edit)	1.703 \pm 0.123	1.290 \pm 0.287	0.504 \pm 0.218	17.380 \pm 2.853	16.764 \pm 4.256	1.416 \pm 0.136	1.037 \pm 0.319
biolord	2.261 \pm 0.000	2.277 \pm 0.137	/	20.420 \pm 6.117	22.210 \pm 10.198	3.418 \pm 1.693	1.444 \pm 0.641
Cinema-OT	2.784 \pm 0.189	2.839 \pm 0.320	1.414 \pm 0.290	13.078 \pm 5.379	24.800 \pm 10.770	1.440 \pm 0.128	1.813 \pm 0.307
scGen	3.544 \pm 0.109	3.778 \pm 0.372	0.981 \pm 0.118	5.742 \pm 1.091	3.615 \pm 1.817	3.859 \pm 3.268	1.215 \pm 0.312
CVAE	0.922 \pm 0.028	0.911 \pm 0.015	1.398 \pm 0.616	1.046 \pm 0.054	0.926 \pm 0.082	1.102 \pm 0.266	1.303 \pm 0.429
CVAE-FM (decode)	0.944 \pm 0.031	0.816 \pm 0.121	1.235 \pm 0.449	1.015 \pm 0.039	0.921 \pm 0.104	0.989 \pm 0.248	1.154 \pm 0.307
CVAE-FM (edit)	0.942 \pm 0.070	0.933 \pm 0.100	1.268 \pm 0.435	0.990 \pm 0.076	0.892 \pm 0.140	1.032 \pm 0.311	1.166 \pm 0.294

D.10. Case study: controlled single-cell editing for enhanced drug response

Figures 14 & 15 show the cell population after editing appeared similar to the populations which responded to the treatment, in both rMMD and gene-expression changes

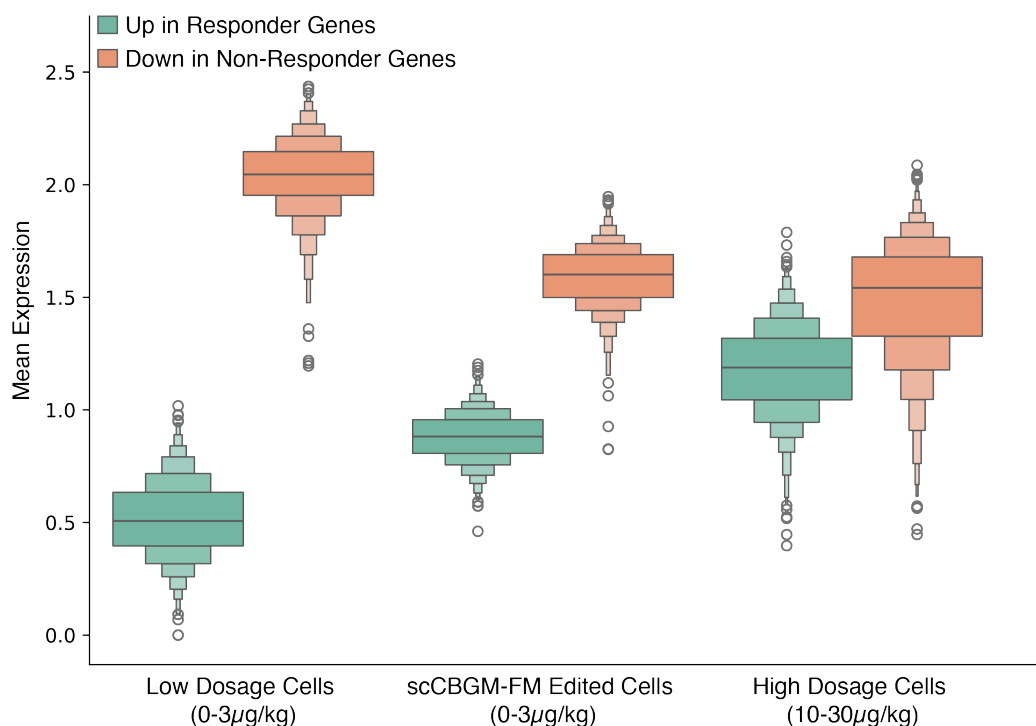


Figure 14. **Gene expression trends under in-silico perturbation in the Nault et al. (2023) dataset.** The distribution of mean expression values (averaged across cells in each group) for the top 100 upregulated (green) and downregulated (orange) marker genes. The edited cells (center) successfully reproduce the target gene signatures, shifting the expression of responder and non-responder genes towards the levels observed in the true high-dosage cells, complementing the global results in Figure 5. We note that only 40 of these marker genes overlap with the total set of top 100 genes defining the manipulated pathway concepts (500 total). The successful recovery of the remaining 80% suggests that the model captures downstream regulatory effects beyond the direct inputs.

D.11. Cell subtype accuracy

To complement our benchmark, we evaluate whether edited cells from a given model preserve their subtype s . For each edited cell in the Kang et al. (2017) dataset, we predict its subtype using a kNN classifier with $k = 15$ neighbors. In Table 24, we report the predicted subtype accuracy (mean \pm SEM) for different models used to edit the cells. scCBGM(-FM) achieves again the best performance over most cell types. As expected, models that achieved an rMMD ≤ 1 show high accuracy (rMMD ≤ 1 means that the predicted counterfactual distribution is closer to the target than any other cell-type distribution in the data). However, we note that high subtype accuracy does not necessarily lead to successful counterfactual predictions. Indeed, the predicted distribution may be closest to the correct subtype distribution but not necessarily overlap.

Table 24. Subtype Prediction Accuracy (Mean \pm SEM) per subtype for different models on the Kang et al. (2017) dataset (**best**, **second-best**, and **third-best** models bolded).

Model	B-cells		CD14		CD4 T cells		CD8 T cells		Dendritic		FCGR3A+		NK cells	
	Type 0	Type 1	Type 0	Type 1	Type 0	Type 1	Type 0	Type 1	Type 0	Type 1	Type 0	Type 1	Type 0	
scCBGM	0.996 \pm 0.001	0.822 \pm 0.008	0.990 \pm 0.000	0.222 \pm 0.045	0.983 \pm 0.002	0.863 \pm 0.007	0.734 \pm 0.011	0.980 \pm 0.001	0.546 \pm 0.007	0.973 \pm 0.003	0.710 \pm 0.006	0.769 \pm 0.043	0.106 \pm 0.009	0.992 \pm 0.001
scCBGM-FM (decode)	0.996 \pm 0.000	0.817 \pm 0.014	0.988 \pm 0.003	0.139 \pm 0.028	0.985 \pm 0.002	0.837 \pm 0.011	0.730 \pm 0.007	0.972 \pm 0.004	0.552 \pm 0.005	0.958 \pm 0.004	0.722 \pm 0.006	0.786 \pm 0.037	0.121 \pm 0.005	0.980 \pm 0.002
scCBGM-FM (edit)	0.996 \pm 0.001	0.833 \pm 0.006	0.988 \pm 0.001	0.306 \pm 0.053	0.983 \pm 0.001	0.881 \pm 0.005	0.745 \pm 0.006	0.975 \pm 0.001	0.551 \pm 0.008	0.948 \pm 0.004	0.682 \pm 0.000	0.876 \pm 0.018	0.093 \pm 0.007	0.960 \pm 0.002
Vanilla-FM (decode)	0.338 \pm 0.014	0.020 \pm 0.002	0.802 \pm 0.014	0.028 \pm 0.028	0.474 \pm 0.009	0.125 \pm 0.007	0.008 \pm 0.002	0.412 \pm 0.011	0.065 \pm 0.005	0.033 \pm 0.005	0.028 \pm 0.006	0.108 \pm 0.004	0.011 \pm 0.003	0.990 \pm 0.001
Vanilla-FM (edit)	0.425 \pm 0.026	0.450 \pm 0.014	0.812 \pm 0.015	0.306 \pm 0.053	0.858 \pm 0.005	0.468 \pm 0.006	0.281 \pm 0.022	0.825 \pm 0.012	0.362 \pm 0.009	0.044 \pm 0.021	0.131 \pm 0.025	0.164 \pm 0.025	0.056 \pm 0.004	0.967 \pm 0.004
CVAE	0.988 \pm 0.001	0.833 \pm 0.006	0.990 \pm 0.001	0.111 \pm 0.000	0.970 \pm 0.002	0.844 \pm 0.003	0.738 \pm 0.008	0.945 \pm 0.006	0.444 \pm 0.010	0.904 \pm 0.008	0.648 \pm 0.007	0.983 \pm 0.001	0.142 \pm 0.005	0.922 \pm 0.001

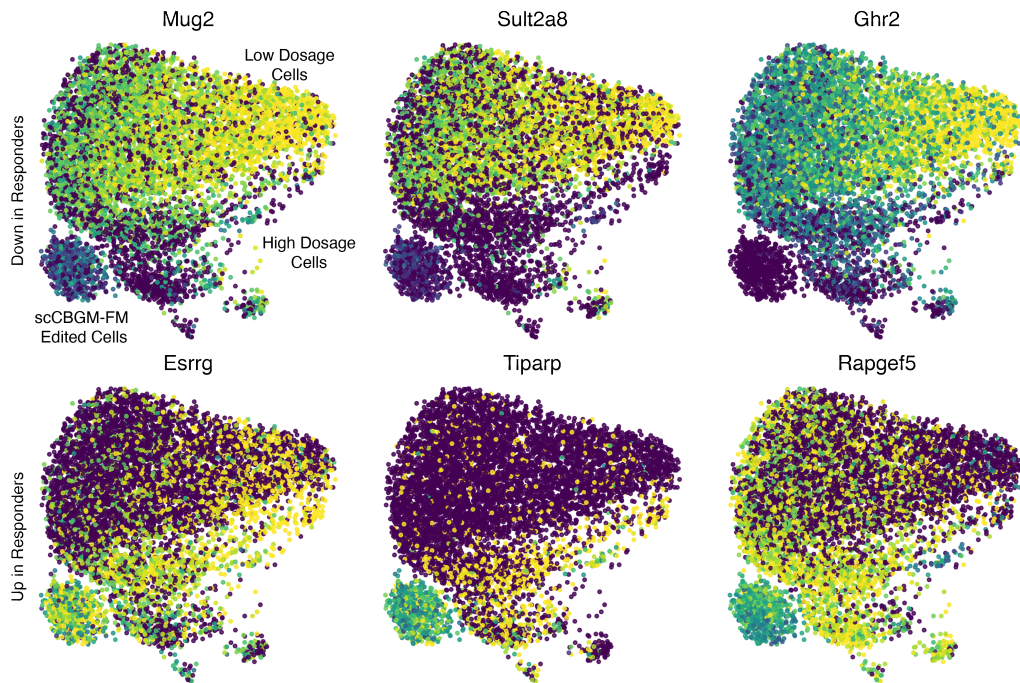


Figure 15. Predicted gene expression trends match experimental ground truth. UMAP visualizations of representative genes from the top 100 differentially expressed set analyzed in Figure 14. **Top row:** Genes downregulated in responders exhibit high expression (yellow) in low-dosage cells but are correctly suppressed in the edited population. **Bottom row:** Genes upregulated in responders are activated in the edited cells, shifting from the low-dosage state (purple) to the high-dosage phenotype (yellow). These patterns confirm that scCBGM-FM drives granular gene-specific shifts consistent with the aggregate trends.

E. Reproducibility Statement

We provide code and notebooks to fully reproduce all results, figures, and tables in a public GitHub repository: <https://github.com/almaan/conceptlab/tree/mlgenx> All data used in this work are publicly available; for convenience, we also share the processed files through an anonymous OSF repository: https://osf.io/kfqj8/?view_only=02cfaddc86da47d5b8fca0577628ddf7.